

INVESTIGATION AND CHARACTERIZATION OF MICROLENSSES FOR IMAGING  
RECEPTION IN INDOOR OPTICAL WIRELESS COMMUNICATIONS

by

Daniel Guerrero

B.A.Sc., The University of British Columbia, 2013

A THESIS SUBMITTED IN PARTIAL FULFILLMENT OF  
THE REQUIREMENTS FOR THE DEGREE OF

MASTER OF APPLIED SCIENCE

in

THE COLLEGE OF GRADUATE STUDIES

(Electrical Engineering)

THE UNIVERSITY OF BRITISH COLUMBIA

(Okanagan)

December 2019

© Daniel Guerrero, 2019

The following individuals certify that they have read, and recommend to the College of Graduate Studies for acceptance, a thesis/dissertation entitled:

INVESTIGATION AND CHARACTERIZATION OF MICROLENSSES FOR IMAGING RECEPTION IN INDOOR OPTICAL WIRELESS COMMUNICATIONS

---

submitted by Daniel Guerrero in partial fulfillment of the requirements of

the degree of Master of Applied Science .

Dr. Jonathan Holzman, School of Engineering

---

**Supervisor**

Dr. Richard Klukas, School of Engineering

---

**Supervisory Committee Member**

Dr. Ian Foulds, School of Engineering

---

**Supervisory Committee Member**

Dr. Sina Kheirkhah, School of Engineering

---

**University Examiner**

## **Abstract**

The gain in popularity of optical wireless technologies over the past decade is the start of a revolution in optical technology. While we have seen commercial optical communication systems firmly establish themselves over the past decades, through the use of optical fibres for point-to-point optical communications, we are now beginning to see the emergence of mobile optical wireless technologies. Such technologies typically use portable imaging receivers and fixed indoor transmitters, such that data can be piggybacked onto lighting from distributed light emitting diodes (LEDs) within the room. These optical wireless communication systems can potentially provide high-speed optical communications with wireless mobility. However, such systems have practical challenges for the imaging receivers, in that they are typically implemented with bulky (typically centimetre-scale) optical elements with narrow field-of-view characteristics. The proposed work addresses these practical challenges by introducing microlens technologies that are suited for optical wireless implementations. It is shown that the implemented microlenses can enable compact imaging, with strong signal levels and wide field-of-view characteristics.

## **Lay Summary**

The research carried out in this thesis explores the use of imaging receivers in indoor optical wireless applications. The key goals are to explore limitations in the imaging receiver brought by the optical elements used to focus the light on to the imaging sensor. Optical wireless systems have a tremendous potential to provide high speed communication by using the existing indoor lighting infrastructure by using modern LEDs. This motivates the initial research into optical wireless applications which leads to this thesis. In the process, a fabrication technique is developed for achieving this goal and allows for characterization and analysis of different imaging receivers.

## **Preface**

The work carried out through this thesis was done under the supervision of Dr. Jonathan Holzman at the Integrated Optics Laboratory of the University of British Columbia's Okanagan campus.

Much of the work carried out in Chapter 3 was based upon a project with an industry partner named Recon Instruments Inc., now Intel Corp. The year-long work was carried out to develop a technology for compact imaging via customized microlens arrays. This work was not published. It was instead delivered to Recon Instruments Inc. as a proof-of-concept study to allow them to replace their existing technology, based upon thermal reflow of microlenses. The project managers were very interested in the findings and continued their work with the Integrated Optics Laboratory, largely through the work of the graduate student Weicheng (Alec) Yan.

The work in Chapter 4 involved the construction of optical wireless imaging receivers. The work was carried out largely by me, with the help of X. Jin. I was the principal investigator for the development of the fabrication system and the supporting software for processing images in the receivers.

# Table of Contents

<b>Abstract.....</b>	<b>iii</b>
<b>Lay Summary .....</b>	<b>iv</b>
<b>Preface.....</b>	<b>v</b>
<b>Table of Contents .....</b>	<b>vi</b>
<b>List of Tables .....</b>	<b>viii</b>
<b>List of Figures.....</b>	<b>ix</b>
<b>List of Symbols .....</b>	<b>xix</b>
<b>Acknowledgements .....</b>	<b>xx</b>
<b>Dedication .....</b>	<b>xxi</b>
<b>Chapter 1: Introduction .....</b>	<b>1</b>
1.1    Optical Wireless Communication Systems .....	3
1.1.1    Point-to-Point Optical Wireless Communication Systems .....	3
1.1.2    Distributed Optical Wireless Communication Systems.....	5
1.2    Optical Wireless Receivers .....	7
1.3    Literature Review.....	10
1.4    Scope of Thesis .....	13
<b>Chapter 2: Analyses of Microlenses .....</b>	<b>15</b>
2.1    Analysis of a Microlens on a Thick Substrate .....	15
2.2    Analysis of a Microlens on a Thin Substrate .....	23
2.3    Analysis of a Microlens under a Thin Substrate .....	29

2.4	Discussion .....	34
<b>Chapter 3: Fabrication of Microlenses .....</b>		<b>37</b>
3.1	Microlens Fabrication System .....	40
3.1.1	Dispensing Sub-System .....	44
3.1.2	Actuation Sub-System .....	45
3.2	Microlens Implementations.....	50
3.2.1	The Low-Contact-Angle (LCA) Microlens .....	50
3.2.2	The High-Contact-Angle (HCA) Microlens.....	52
3.2.3	The Low-Contact-Angle (LCA) Microlens Array .....	53
3.3	Discussion on Reproducibility .....	56
<b>Chapter 4: Application of Microlenses to Imaging Receivers .....</b>		<b>58</b>
4.1	Imaging Receivers.....	58
4.2	Optical Wireless Polar Angle Imaging Testbed.....	64
4.3	Characterizations of the Imaging Receivers in the Optical Wireless Testbed .....	65
4.3.1	Imaging Receiver with the Low-Contact-Angle (LCA) Microlens.....	65
4.3.2	Imaging Receiver with the High-Contact-Angle (HCA) Microlens.....	67
4.3.3	Imaging Receiver with the LCA Microlens Array .....	69
4.4	Discussion .....	70
<b>Chapter 5: Conclusion .....</b>		<b>74</b>
<b>Bibliography .....</b>		<b>76</b>
<b>Appendices.....</b>		<b>80</b>
	Appendix A - Lens Aberration Types.....	80
	Appendix B - Microlens Array Fabrication .....	82

## List of Tables

Table 2.1	The focal length, FOV, and focal spot size for the LCA microlens, HCA microlens, and LCA microlens array. The stated focal spot size is the effective diameter of the focal spot at the maximum incident polar angle, i.e., at half the FOV. The microlens diameter, $d$ , is that of the isolated microlenses. .... 36
Table 3.1	Fabrication sub-system parameters for the LCA microlens. The polymer is dispensed for 250ms with a pressure of 60psi while the 32-gauge needle tip is placed 10 $\mu\text{m}$ away from the surface of the glass substrate. After contact of the polymer with the glass substrate in air and the microlens has formed, the UV curing is applied. .... 51
Table 3.2	Fabrication sub-system parameters for the HCA microlens. The polymer is dispensed for 1.5s with a pressure of 60psi while the 32-gauge needle tip is placed 10 $\mu\text{m}$ away from the surface of the glass substrate. The dispensing takes place in a glycerol filler to achieve the desired contact angle. After contact of the polymer with the glass substrate inside the glycerol and the microlens has formed, the UV curing is applied..... 53
Table 3.3	Fabrication sub-system parameters for the LCA microlens array. The polymer is dispensed for 100ms with a pressure of 60psi while the 34-gauge needle tip is placed 10 $\mu\text{m}$ away from the surface of the glass substrate. After contact of the polymer with the glass substrate in air and the microlens has formed, the next element in the array is made. Once all the elements are complete the array is UV cured. .... 55

## List of Figures

- Figure 1.1 A point-to-point OW communication system showing the deployment of two transceivers. Such transceivers are often deployed on rooftops because this environment offers clear line-of-sight channels between transceivers. .... 3
- Figure 1.2 A distributed OW communication system showing the deployment of multiple fixed transceivers, distributed across an overhead grid, and a mobile transceiver, which is free to move throughout the indoor environment. Such a system benefits from having multiple communication channels, as this diminishes the effects of pointing errors and shadowing..... 6
- Figure 1.3 Two forms of OW receivers below LED transmitters. The (a) standard photodiode receiver captures contributions of incident optical power from both LED transmitters, and is unable to spatially discriminate these contributions, while the (b) imaging receiver is able to distinguish the contributions of incident optical power from the two transmitters..... 8
- Figure 2.1 Cross-sectional profile of a microlens on a thick substrate. It has a diameter of  $d$ , radius of curvature of  $R$ , contact angle of  $\alpha$  around its perimeter, and sag of  $s$ , being the thickness of the microlens on the OA. The microlens and substrate both have a refractive index of  $n$ . The coordinates  $(x,z)$  are defined with respect to an origin at the intersection of the planar surface and the OA. Two light rays run parallel to the OA at the top of the figure and intersect the OA at the focal point. The distance along the OA from the origin to the focal point is the focal length,  $f$ ..... 16

Figure 2.2 Ray-tracing simulations of microlenses with a diameter of  $d$  on an infinitely thick substrate. where the microlens and substrate both have a refractive index of  $n = 1.5$ . The system is shown for the (a) LCA microlens with a contact angle of  $\alpha = 30^\circ$  and rays at an incident polar angle of  $\theta = 0^\circ$ , (b) LCA microlens with a contact angle of  $\alpha = 30^\circ$  and rays at an incident polar angle of  $\theta = 16^\circ$ , (c) HCA microlens with a contact angle of  $\alpha = 90^\circ$  and rays at an incident polar angle of  $\theta = 0^\circ$ , and (d) HCA microlens with a contact angle of  $\alpha = 90^\circ$  and rays at an incident polar angle of  $\theta = 28.5^\circ$ . ..... 20

Figure 2.3 Imaging characteristics of a microlens on a thick substrate showing the (a) normalized focal length,  $f/d$ , and (b) FOV versus the contact angle,  $\alpha$ . For an increasing contact angle in (a), the normalized focal length transitions from a hyperbola,  $f(\alpha \ll 90^\circ)/d \approx 2/\alpha$ , to a constant of  $f(\alpha \approx 90^\circ)/d \approx 1$ . For increasing contact angle in (b), the FOV transitions from a linear trend,  $\text{FOV}(\alpha \ll 90^\circ) \approx \alpha$ , to a constant of  $\text{FOV}(\alpha \approx 90^\circ) \approx 53.13^\circ$ . Data points for the LCA microlens with  $\alpha = 30^\circ$  and the HCA microlens with  $\alpha = 90^\circ$  are enclosed by red and blue circles, respectively. .... 22

Figure 2.4 Cross-sectional profile of a microlens on a thin substrate. The microlens has a diameter of  $d$ , radius of curvature of  $R$ , contact angle of  $\alpha$  around its perimeter, and sag of  $s$ , being the thickness of the microlens on the OA. The substrate has a thickness of  $t$ . The microlens and substrate both have a refractive index of  $n$ . The coordinates  $(x,z)$  are defined with respect to an origin at the intersection of the top planar surface and the OA. Two light rays

run parallel to the OA at the top of the figure and intersect the OA at the focal point. The distance from the origin to the focal point is the focal length,  $f$ ... 23

Figure 2.5 Ray-tracing simulations of microlenses with a diameter of  $d$  on a thin substrate with a normalized thickness of  $t/d = 0.2$ , where the microlens and substrate both have a refractive index of  $n = 1.5$ . The system is shown for the (a) LCA microlens with a contact angle of  $\alpha = 30^\circ$  and rays at an incident polar angle of  $\theta = 0^\circ$ , (b) LCA microlens with a contact angle of  $\alpha = 30^\circ$  and rays at an incident polar angle of  $\theta = 14.2^\circ$ , (c) HCA microlens with a contact angle of  $\alpha = 90^\circ$  and rays at an incident polar angle of  $\theta = 0^\circ$ , and (d) HCA microlens with a contact angle of  $\alpha = 90^\circ$  and rays at an incident polar angle of  $\theta = 21.5^\circ$ . ..... 25

Figure 2.6 Imaging characteristics of a microlens on a thin substrate showing the (a) normalized focal length,  $f/d$ , and (b) FOV versus the contact angle,  $\alpha$ , given a microlens with a diameter of  $d$ , a substrate with a normalized thickness of  $t/d = 0.2$ , and a refractive index of  $n = 1.5$ . The prior results for a microlens on a thick substrate are also shown. According to (a) and (b), an increasing contact angle yields a shorter normalized focal length and a wider FOV. Data points for the LCA microlens with  $\alpha = 30^\circ$  and the HCA microlens with  $\alpha = 90^\circ$  are enclosed by red and blue circles, respectively. .... 27

Figure 2.7 Cross-sectional profile of a microlens under a thin substrate. The microlens has a diameter of  $d$ , radius of curvature of  $R$ , contact angle of  $\alpha$  around its perimeter, and sag of  $s$ , being the thickness of the microlens on the OA. The

substrate has a thickness of  $t$ . The microlens and substrate both have a refractive index of  $n$ . The coordinates  $(x,z)$  are defined with respect to an origin at the intersection of the bottom planar surface and the OA. Two light rays run parallel to the OA at the top of the figure and intersect the OA at the focal point. The distance from the origin to the focal point is the focal length,  $f$ . ..... 30

Figure 2.8 Ray-tracing simulations of microlenses with a diameter of  $d$  under a thin substrate with a normalized thickness of  $t/d = 0.2$ , where the microlens and substrate both have a refractive index of  $n = 1.5$ . The system is shown for the (a) LCA microlens with a contact angle of  $\alpha = 30^\circ$  and rays at an incident polar angle of  $\theta = 0^\circ$ , (b) LCA microlens with a contact angle of  $\alpha = 30^\circ$  and rays at an incident polar angle of  $\theta = 13^\circ$ , (c) HCA microlens with a contact angle of  $\alpha = 90^\circ$  and rays at an incident polar angle of  $\theta = 0^\circ$ , and (d) HCA microlens with a contact angle of  $\alpha = 90^\circ$  and rays at an incident polar angle of  $\theta = 26^\circ$ . ..... 31

Figure 2.9 Imaging characteristics of a microlens under a thin substrate showing the (a) normalized focal length,  $f/d$ , and (b) FOV versus the contact angle,  $\alpha$ , given a microlens with a diameter of  $d$ , a substrate with a normalized thickness of  $t/d = 0.2$ , and a refractive index of  $n = 1.5$ . The prior results for a microlens on a thick substrate and a microlens on a thin substrate are also shown. According to (a) and (b), an increasing contact angle yields a shorter normalized focal length and a wider FOV. Data points for the LCA microlens with  $\alpha = 30^\circ$  and

HCA microlens with  $\alpha = 90^\circ$  are enclosed by red and blue circles, respectively. .... 33

Figure 3.1 Cross-sectional profile of a representative microdroplet. The liquid microdroplet has a diameter of  $d$ , radius of curvature of  $R$ , contact angle of  $\alpha$  around its perimeter, and sag of  $s$ , being the thickness of the microlens at its centre. The substrate has a thickness of  $t$ . The surrounding medium is an ambient filler. The coordinates  $(x,z)$  are defined with respect to an origin at the intersection of the bottom planar surface and the OA. The three-phase contact line is shown with the solid-filler interfacial energy,  $\gamma_{sf}$ , the solid-liquid interfacial energy,  $\gamma_{sl}$ , and the liquid-filler interfacial energy  $\gamma_{lf}$ ..... 39

Figure 3.2 The microlens fabrication system. The system is comprised of a control unit, a syringe barrel containing a piston and the NOA 68 polymer, onto which is attached to the needle tip, and a dispensing container. The dispensing container houses a filler solution, if needed. The microdroplet is dispensed within the dispensing container. .... 42

Figure 3.3 Transmissivity of NOA 68 polymer (as a percent) versus wavelength (in nm). The polymer exhibits low transmission (and thus high absorption) below wavelengths of 420 nm, and for this reason a wavelength of 405 nm is used to cure it. It exhibits high transmission (and thus low absorption) across the visible and near-infrared spectrum, and for this reason it can be used for broadband operation of imaging receivers. The data shown here was provided by Norland Products Inc. .... 42

Figure 3.4 The microlens dispensing system shown as photographs of (a) the overall system, including the syringe barrel that dispenses the polymer microdroplet and the optical fibre that delivers the UV beam to cure it, and (b) the needle tip that dispenses the polymer to form a microdroplet on the glass substrate. 43

Figure 3.5 The LabVIEW graphical user interfaces for (a) the dispensing sub-system, which controls dispensing polymer into a microdroplet, and (b) the actuation subsystem, which translates the needle tip. .... 43

Figure 3.6 Microlens diameter,  $d$ , versus dispensing pressure for dispensing in an ambient (filler) of (a) air and (b) glycerol. A dispensing time of 100 ms is denoted by open circles with a grey trendline; a dispensing time of 250 ms is denoted by crosses with an orange trendline. The dispensing is carried out with a 34-gauge needle tip. .... 46

Figure 3.7 Steps of the actuation sub-system for a microdroplet with a relatively high contact angle, due to a relatively large separation between the needle tip and the glass substrate. The steps include (a) substrate raising, (b) microdroplet dispensing, (c) pausing, (d) substrate lowering, and (e) UV-curing. .... 48

Figure 3.8 Steps of the actuation sub-system for a microdroplet with a relatively low contact angle, due to a relatively large separation between the needle tip and the glass substrate. The steps include (a) substrate raising, (b) microdroplet dispensing, (c) pausing, (d) substrate lowering, and (e) UV-curing. .... 48

Figure 3.9 The fabricated LCA microlens as characterized by its (a) photograph, and (b) ray-tracing simulation. The profiles of these two match closely with a total diameter of  $d = 790 \mu\text{m}$ . .... 51

Figure 3.10	The HCA microlens as characterized by its (a) photograph and (b) ray-tracing simulation. The profiles of these two match closely with a total diameter of $d = 810 \mu\text{m}$ .	53
Figure 3.11	The LCA microlens array as characterized by its (a) photograph and (b) ray-tracing simulation. The microlens photograph shown is a representative 5x5 microlens array. In characterization, the 3x3 internal microlens array is used for characterization and comparison with the other microlens implementations. In this case, the focal distance seen in the ray-tracing simulations has proportionally decreased focal length due to the smaller diameter.	55
Figure 3.12	Histograms showing the counts for diameters of 100 dispensed LCA and 100 dispensed HCA microlenses. The LCA microlenses denoted by the blue bars show good precision and good accuracy, with values close to the targeted diameter of $d = 230 \mu\text{m}$ . The HCA microlenses denoted by the orange bars show poor precision and poor accuracy, given their wide variations and heightened values for the diameters.	57
Figure 4.1	Configurations of the imaging receivers showing the image sensor below the (a) LCA microlens, (b) HCA microlens, and (c) LCA microlens array. The configurations show illumination of the microlenses by light rays that are parallel to the optical axis (in grey) and light rays that are oblique to the optical axis (in red). The oblique rays focus on the image sensor at the outermost edge of the microlens perimeter.	59

Figure 4.2 Photograph of the OV7720 image sensor. It captures images at a frame rate of 187 frames-per-second and has pixels with a cross-sectional area of  $6\ \mu\text{m} \times 6\ \mu\text{m}$ . ..... 59

Figure 4.3 Data structure for the images captured by the image sensor. The captured images are stored as two-dimensional arrays of RGB values at each frame in time. The frames are denoted by  $t_0, t_1, \dots, t_{N-1}$ , where the total number of frames is  $N$ . For each RGB array at a given frame in time, the integers  $i$  and  $j$  denote pixel coordinates along the horizontal and vertical dimensions, respectively. .... 60

Figure 4.4 Intensity profiles (in red shading) on the image sensor from ray-tracing analyses for illumination at the polar angle of  $\theta = 0^\circ$  and the polar angle at the edge of the FOV, being  $\theta = 26^\circ, 56^\circ$ , and  $26^\circ$  for the (a) LCA microlens, (b) HCA microlens, and (c) LCA microlens array, respectively. The results are displayed roughly to scale with a grid of pixels having an area of  $6\ \mu\text{m} \times 6\ \mu\text{m}$ . .... 61

Figure 4.5 Intensity profiles of two neighbouring LED transmitters focused on the imaging sensor. The top row shows the intensity profiles as viewed from above; the bottom row shows the intensity profiles as viewed in a profile. We see cases here where (a) the two objects are clearly distinguishable, (b) the objects overlap but are still distinguishable, and (c) the two objects produce overlapped images. .... 63

Figure 4.6 (a) The polar angle imaging testbed with the 30 LEDs transmitters above an imaging receiver. (b) The image sensor integrated with the fabricated microlenses to make the imaging receiver..... 64

Figure 4.7 The LCA microlens's (a) SEM image, showing its small contact angle ( $27^\circ$ ) and large diameter ( $790\ \mu\text{m}$ ), and (b) ray-tracing simulation. The microlens was fabricated with a 32-gauge needle tip and 60 psi of pressure for 250 ms. This LCA microlens yields a long and narrow focal characteristic..... 65

Figure 4.8 A representative image captured by the image sensor using the LCA microlens. The LCA microlens is capable of resolving sharp focal spots for the displayed five LEDs, but the four LEDs on the corners cannot be captured in the image..... 66

Figure 4.9 The HCA microlens's (a) SEM image, showing its large contact angle and large diameter ( $760\ \mu\text{m}$ ), and (b) ray-tracing simulation. The microlens was fabricated with a 34-gauge needle tip and 60 psi of pressure for 1 s. This HCA microlens yields a short and wide focal characteristic..... 68

Figure 4.10 A representative image captured by the image sensor using the HCA microlens. The HCA microlens is capable of resolving sharp focal spots for the displayed five LEDs, but the four LEDs on the corners are not accurately resolved due to aberration..... 68

Figure 4.11 A representative image captured by the image sensor using the LCA microlens array. The LCA microlens array is capable of resolving all the LED transmitters, although their images show large signs of overlap from adjacent microlenses in the array. .... 69

Figure 4.12 Intensity profile of the captured image with the LCA microlens being implemented in the imaging receiver. This LCA microlens implementation leads to a large spread on the image sensor for the transmitters on the polar angle testbed. This makes it relatively easy for the image sensor to distinguish between neighbouring transmitters as there is a clearly distinguishable peak for each transmitter. .... 71

Figure 4.13 Intensity profile of the captured image with the HCA microlens being implemented in the imaging receiver. This HCA microlens implementation leads to a small spread on the image sensor for the transmitters on the polar angle testbed. However, these spots have smaller peak intensities than those of the LCA due to their aberration and greater spread of power in the focal spot. This makes it more challenging to image process. The challenge arises because it becomes difficult to distinguish between neighbouring transmitters and there is a stronger background level noise (giving a smaller dynamic range). .... 72

Figure 4.14 Intensity profile of the captured image with the LCA microlens array being implemented in the imaging receiver. This implementation captures an image with a 3×3 microlens array, with each microlens projecting an image of the transmitters on the polar angle testbed. The replication and overlap of these images can make the signal processing difficult..... 73

## List of Symbols

Symbol	Description
$\alpha$	Contact angle
$\phi$	Incident azimuthal angle
$\theta$	Incident polar angle
$n$	Refractive index
$d$	Microlens diameter
$R$	Radius of curvature
$s$	Sag
$f(\alpha)$	Focal length as a function of contact angle
$f(\alpha)/d$	F-number as a function of contact angle
$\text{FOV}(\alpha)$	Field of view as a function of contact angle
$\gamma_{\text{sf}}$	Solid-filler interfacial energy
$\gamma_{\text{sl}}$	Solid-liquid interfacial energy
$\gamma_{\text{lf}}$	Liquid-filler interfacial energy

## **Acknowledgements**

It is great to have opportunity to thank all the individuals that I have had the pleasure to work with and learn from, you have inspired me.

First and foremost, Dr. Jonathan Holzman and his leadership and guidance. His enthusiasm with learning and teaching is contagious in the most motivating ways. In addition, I would like to thank Dr. Klukas, for his time with the optical wireless development and insight into solving challenges. I would like to thank my entire committee.

Next, I want to thank all the members I worked with at the Integrated Optics Lab. It's been a pleasure working with and learning with you all. A special and important thank you and acknowledgement goes out to Xian Jin. In addition, I would like to thank my colleagues Mark Bergen, Blago Hristovski, Naomi Freeden, Hugo Chaves, and Alec Yan for help with projects. Also all my other colleagues that made a important part of my time in the Lab, such as Brandon Born, Christopher Collier, Jackie Nichols, and Emily Landry.

## Dedication

*This thesis is dedicated to my mother, wife, and kids...*

*for their endless support and encouragement.*

## Chapter 1: Introduction

Mobile devices are witnessing demands for faster and faster data rates. This has manifested itself as a doubling of data rates every 18 months [1]. The demands have been met so far by existing radio frequency (RF) wireless technologies, although the RF spectrum is a limited (and increasingly congested) commodity. Researchers to date, have mitigated RF congestion by using increasingly complicated modulation formats, such as high-order quadrature amplitude modulation (QAM), e.g., 512-QAM [2]. However, there are few remaining contiguous licensed bands below 300 GHz, and spectral scarcity is becoming a major concern.

Optical wireless (OW) technology emerged in response to the above demands and challenges [3, 4]. Such OW technology benefits from wireless mobility, unlicensed bands, and the tremendous data rates that can be achieved via modulation of optical and infrared carrier frequencies, which span into the hundreds of terahertz. In fact, it was this latter benefit that spurred the emergence of long-haul optical fibre systems, which have become the backbone of the modern Internet.

It is important to note that OW technology differs greatly from optical fibre technology in terms of its implementation and challenges. Optical fibre technology enables long-haul point-to-point data transmission with little concern to optical attenuation, due to its use of repeaters and erbium doped fibre amplifiers [5], and little attention paid to ambient noise, because of its strong containment of light within its core. Given the strong signal-to-noise ratios (SNR) that can be achieved by optical fibre systems, the remaining challenges for these systems pertain to speed. There is an ongoing pursuit to minimize signal dispersion within the optical

fibre and minimize the response time of front-end optoelectronics for greater and greater data rates. Optical wireless technology is in stark contrast to this. It is susceptible to optical attenuation and ambient noise due to its implementation within the open (typically indoor) communication environment. The alignment of transmitters and receivers, and the presence of surrounding optical sources, can all diminish the SNR. Thus, it is important for receivers in OW communication systems to consider the view of their environment.

The metrics of OW communication systems must be carefully considered in the design and implementation of the systems' transmitters and receivers. The OW transmitters are often implemented in tandem with room lighting, which typically makes use of light emitting diodes (LEDs) [6]. Such a scheme benefits from its energy efficiency because there is no longer a need for independent broadcasting of RF energy. The OW receivers are often implemented as standard photodiode receivers or imaging receivers [7, 8]. Imaging receivers carry out optoelectronic detection, like standard photodiode receivers, but unlike photodiodes they are able to distinguish signals from a multitude of distributed transmitters. Such a capability can offer reduced bit-error rates, by having multiple transmitters employing diversity reception [9], and/or greater data rates, by having multiple transmitters carrying out multiplexing [10]. The remainder of this chapter provides details on OW communication systems, OW receivers, and the scope of this thesis—in offering improvements to OW communication systems and OW receivers.

## 1.1 Optical Wireless Communication Systems

Optical wireless communication systems can be realized in two general implementations. There are point-to-point OW communication systems, which typically use laser transmitters over long-range outdoor links, and there are distributed OW communication systems, which typically use LED transmitters over short-range indoor links. The details of these two implementations are described in the following subsections.

### 1.1.1 Point-to-Point Optical Wireless Communication Systems

Point-to-point OW communication systems are implemented with direct data transmission from one transmitter to one receiver, or from one transceiver to another transceiver for bi-directional communication. A schematic of this point-to-point optical communication system is shown in Figure 1.1. The figure shows a simple laser link between roof-top transceivers.

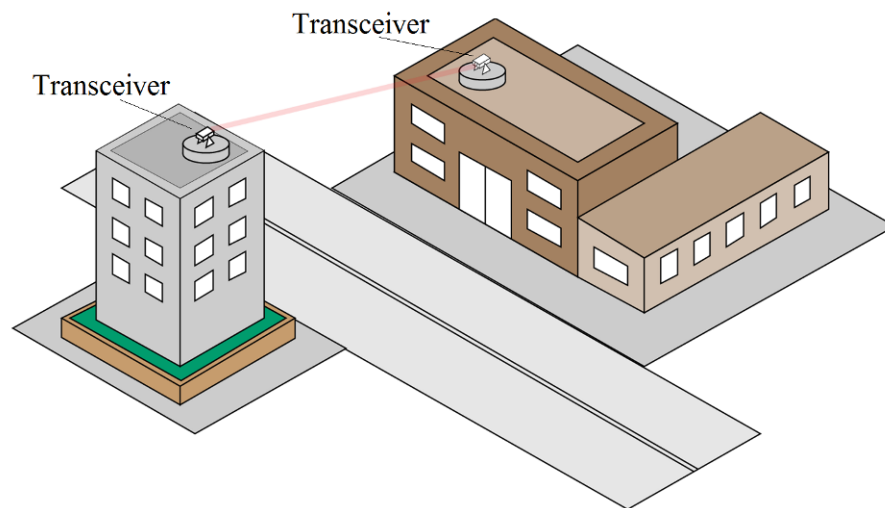


**Figure 1.1 A point-to-point OW communication system showing the deployment of two transceivers. Such transceivers are often deployed on rooftops because this environment offers clear line-of-sight channels between transceivers.**

The typical transmitter that is used for laser-based point-to-point OW communication systems includes a laser and telescope. The laser generates the coherent beam, and the telescope expands and collimates the beam for transmission to the remote receiver. This can enable effective long-range data transmission through the outdoor environment. The data is encoded onto the beam via amplitude modulation or phase modulation for analog transmission or via amplitude-shift keying or phase-shift keying for digital transmission, although it is also possible to encode data via amplitude and phase simultaneously to implement higher-order quadrature amplitude modulation. The transmitted beam can have its wavelength lie within the visible spectrum, spanning wavelengths between 400 nm to 700 nm, or within the infrared spectrum, spanning between 700 nm and 1 mm. However, attention must be paid to the chosen wavelength's susceptibility to atmospheric absorption and scattering, as well as eye safety constraints. Fortunately, the 1550 nm wavelength used for most optical-fibre-based communication systems, because of its minimal dispersion, also offers transmission through the atmosphere with relatively low susceptibility to absorption and scattering. At the same time, it has especially low constraints due to eye safety.

The typical receiver that is used for OW communication systems makes use of one or more photodiodes to provide optoelectronic conversion. As such, the optical data in the received laser beam is translated into an electrical signal. However, care must be taken to ensure that the photodiode is well matched to the wavelength of the transmitter. This is done by selecting a photodiode with an especially high responsivity. Care must also be taken to ensure that the photodiode has a sufficiently small capacitance. This leads to a correspondingly small resistance-capacitance time constant and a broad bandwidth.

Point-to-point OW communication systems have demonstrated impressive performance characteristics. Commercial systems are available that can achieve a full duplex channel at 2.3 Gbit/s under water over 1 km at a wavelength of 1550 nm [11]. The greatest challenge for point-to-point OW communication systems is their reliance upon direct line-of-sight links. In other words, they cannot easily rely upon multipath scattering for transmission via non-line-of-sight links. This makes such systems susceptible to beam pointing errors [12] and shadowing [13], either of which can degrade or even prevent transmission.

### **1.1.2 Distributed Optical Wireless Communication Systems**

Distributed OW communication systems differ from their point-to-point counterparts in that the optical data is broadcasted from the transmitter over a wide solid angle to a receiver that exists within the transmitter's viewing angle. As such, the distributed system can be implemented with multiple transmitters, each with a wide viewing angle, to spread the data transmission over a wide area. The receiver then, having sufficient field-of-view (FOV), is free to move throughout this area with less concern to pointing errors and shadowing. Having a sufficient wide viewing angle for all the transmitters, and FOV for the receiver increases link reliability. A schematic of a distributed OW communications system is shown in Figure 1.2. The system makes use of multiple fixed transceivers, laid out in an overhead grid, along with a mobile transceiver, which is free to move throughout the indoor environment.

The typical transmitter that is used for the distributed OW communication system is the light emitting diode (LED). The LED is an incoherent optical source that transmits its optical power over a wide solid angle. This is in stark contrast to the aforementioned laser, whose transmission is coherent and emitted within a far narrower solid angle. Thus, the LED is well

suitable to the needs of distributed OW communications systems. However, there are two challenges that must be recognized when using such LEDs. First, LEDs typically offer lower

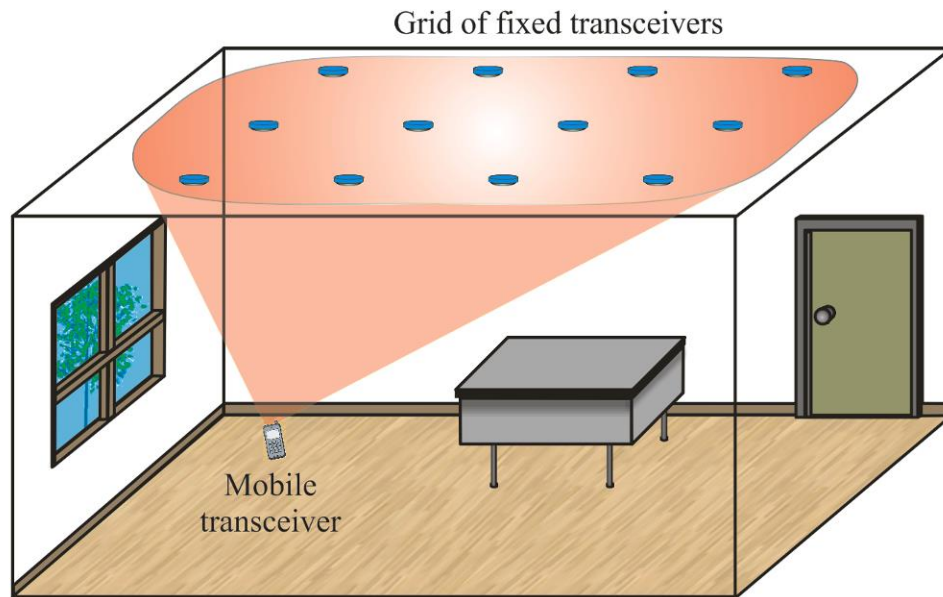


**Figure 1.2 A distributed OW communication system showing the deployment of multiple fixed transceivers, distributed across an overhead grid, and a mobile transceiver, which is free to move throughout the indoor environment. Such a system benefits from having multiple communication channels, as this diminishes the effects of pointing errors and shadowing.**

rates of modulation in comparison to lasers. This is because lasers are resonant structures, with a threshold input current, which allows for rapid and strong modulation of the output power with only a small change in the input current (with a suitable bias current). In contrast, LEDs are typically non-resonant structures with a weaker dependence between the output power and input current. However, it is worth noting, that the growing interest in indoor OW communications has spurred developments in LEDs. Of particular note has been the introduction of the resonant LED, which offers modulation rates up to 800 MHz [14]. Second, LEDs yield lower received powers at the receiver, in comparison to analogous lasers transmitting the same optical power. This is because LEDs spread their transmitted optical

power over a wider area, which results in reduced intensities and lower optical powers at the receiver. With this in mind, it is necessary to consider the signal and noise levels within a distributed OW communication system and design the receiver in such a way that it can achieve an acceptable SNR at the receiver. Such design considerations for the OW receiver are considered in the following section.

## **1.2 Optical Wireless Receivers**

Optical wireless receivers can be implemented with two general forms. The two forms, being the standard photodiode receiver and the imaging receiver, are described in this section.

The standard photodiode receiver is straightforward. It makes use of a single photodiode in the manner shown Figure 1.3(a). The photodiode carries out the necessary optoelectronic conversion to transform the incident optical data into corresponding electrical data. The major benefit of the standard photodiode receiver is its simplicity. The photodiode that is used can be made suitably large, to capture a correspondingly large level of incident optical power, or can be made suitably small, to have a correspondingly small capacitance (and thus a broad bandwidth). The major challenge of the standard photodiode receiver is that it cannot spatially discriminate the received optical data. In other words, it is incapable of spatially distinguishing multiple transmitters. Beams having been sent from multiple transmitters yield powers that are superimposed on the photodiode to create one value of photocurrent. Thus, this standard photodiode receiver cannot exploit the benefits of multiplexing, with which multiple transmitters are used to establish independent communication channels for higher data rates, or the benefits of diversity reception, with which multiple transmitters are used to relay the same data for greater reliability and improved bit-error rates.

The imaging receiver differs from the standard photodiode receiver in that it has many (potentially millions) of individual photodetectors. The photodetectors are typically implemented as pixels within the active region of an image sensor. When a lens is situated above such an image sensor, the system can collect incident optical data in the form of an image. A schematic of an imaging receiver is shown in Figure 1.3(b). Such an

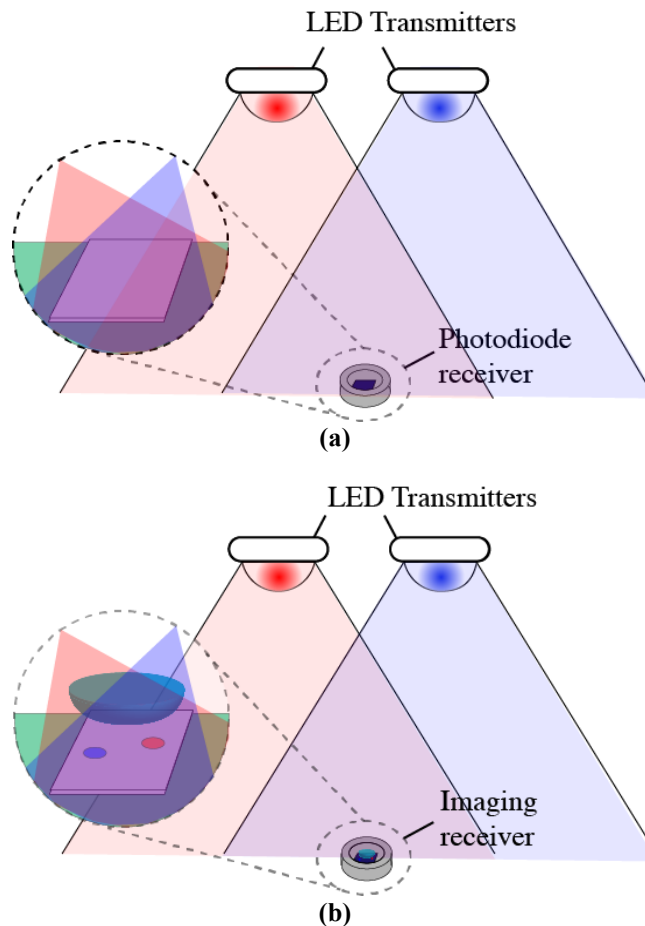


**Figure 1.3 Two forms of OW receivers below LED transmitters. The (a) standard photodiode receiver captures contributions of incident optical power from both LED transmitters, and is unable to spatially discriminate these contributions, while the (b) imaging receiver is able to distinguish the contributions of incident optical power from the two transmitters.**

implementation gives the imaging receiver the ability to separately process data from individual transmitters, which ultimately enables multiplexing and/or diversity reception. However, such imaging receivers must be realized with careful consideration to design goals for practicality and performance. Here, we list one design goal for practicality, and two design goals for performance that are used as benchmarks throughout this thesis.

In terms of the one design goal for practicality, the imaging receiver should have a flat form factor. This means that it should be implemented with a lens having a sufficiently small focal length. Many imaging receivers in the literature to date have made use of optics with centimetre-scale focal lengths [8]. This was done because of the fundamental relationship between the focal length and diameter of the lens. The lens diameters were made large to collect large optical powers and thereby generate appreciable signal levels. In this work, the design goal for practicality (targeting a flat form factor) is quantified by a metric of  $f$ -number, being the ratio of focal length to diameter.

For the first design goal for performance, the imaging receiver should have a broad view of its environment. This allows the receiver to establish simultaneous links with as many transmitters as possible—and ultimately enable operation with multiplexing and/or diversity reception. However, such a demand can be challenging to implement given that a broad view requires a lens with high curvature, i.e., a small radius of curvature, and high curvatures are difficult to implement with sub-millimetre optics. In this work, the first design goal for performance (targeting a broad view of the environment) is quantified by a metric of FOV.

In addition, the second goal for performance is that the lens should have the minimum amount of aberration as possible. Aberration distorts the ideal densely packed focal spot into a dispersed signal over a much larger area. A smaller spot on the image sensor will allow for

denser packed LED transmitters with less susceptibility to crosstalk and noise. Although at the same time, a smaller spot may lead to pixel saturation and clipping, which can be calibrated for by reducing the digital gain of the image sensor. The spot size will be affected by the types of aberration the lens exhibits. In this work, the second design goal for performance is quantified by a metric of the ratio of focal spot size to diameter.

It is apparent that these design goals for practicality and performance in imaging receivers are defined largely by their optics—and the challenges in achieving these goals set the stage for this thesis.

### **1.3 Literature Review**

Due to the potential of OW technologies, there are many research groups advancing the technologies. As such, the literature in this section is divided up into the components of a typical OW link. First, we explore the design of transceivers that are suitable for OW communication with bidirectionality. Second, we explore the state-of-the-art for LED transmitters being used simultaneously for lighting and communications. Last, we explore the fabrication technique used to develop microlenses that can be used in OW imaging receivers.

First, we consider the need for bidirectionality in OW communications. Major efforts for this have been made by the research group at the University of Oxford [3]. The group introduced high-speed integrated transceivers. The transceivers not only allow for high-speed data transmission on the downlink portion of the communication link, but also the ability to transmit high-speed data back to the host. The design of these integrated transceivers includes a custom detector array and a custom emitter array that emits through the

semiconductor, to allow for flip-chip bonding of the arrays to driver electronics. The downlink portion of the OW communication link includes transmitting LEDs, which transmit data to imaging receivers on a mobile device. For this receiver, advancements in integration, for smaller scales, are welcome.

Second, in recognition of the evolution of OW technologies, other research groups have targeted the LED transmitters in an effort to achieve higher bandwidths. As an example, Ferreira *et al.* [6] put forward GaN-based micro-LEDs that are suitable for indoor lighting and OW communications. This continued from their earlier work on LEDs for OW communication, whereby they reduced the LED's active area to decrease capacitance and allow for larger bandwidths. In their latest achievement, shown in [6], micro-LEDs are used with various modulation techniques to further increase the transmission rates of GaN-based LEDs. Their strongest result featured orthogonal frequency division multiplexing with a transmission rate of 5 Gb/s [6]. This is a remarkable achievement given that the LEDs are also suitable for room lighting.

Last, imaging receivers would not be possible if it were not for the optical elements used to focus the distant objects onto the image sensor. Given this fact, microlenses have been introduced into imaging receivers and fabricated using thermal reflow. This technique was first reported in 1988 [15] and has since become a popular choice, as shown by Si Di and Ru-xu Du [16]. The technique uses lithography to create cylinders of photoresist on a glass substrate. It then uses high temperature to melt the photoresist into quasi-spherical shapes resembling microlenses. The technique works well as it leads to smooth surfaces on the microlenses. However, the key drawback of the technique is that it is hard to create a microlens with the high curvature that is needed for a short focal length and low f-number.

Due to the melting process, the contact angles of the microlenses are limited to values below  $25^\circ$ , which produces large focal lengths and f-numbers, which ultimately leads to narrow FOVs. This limits its capabilities for OW technologies, and their implementations, given that such technologies often benefit from wide FOVs. For indoor communications and positioning, for example, it is advantageous to have the microlenses capture as wide of an image as possible of the overhead ceiling, over which the transmitters are deployed, as this allows the receiver to see many LEDs.

Given the abovementioned technologies, there is great potential to improve the imaging performance of OW receivers. The proposed thesis puts forward such improvements by way of the work outlined in the following section.

## 1.4 Scope of Thesis

This thesis puts forward work on the integration and application of microlenses for imaging receivers. Effort is made to develop microlenses and characterize them for use as an imaging receiver in an indoor OW communication test bench. The desired microlens is the one that results in an imaging receiver that functions with a flat form factor for practicality, as defined by the metric of f-number, has a broad view of their environment, as defined by the metric of FOV, and has low aberration, as defined by the metric of focal spot size.

Chapter 1 gave a general introduction to OW systems, and the motivation for exploring such technologies. It described OW point-to-point and distributed links and how the different transmitters play a role. The attention then shifted to the OW receivers, and the difference between a single photodiode and an imaging receiver. The practicality of imaging receivers and their inherent ability to spatially resolve objects and unique transmitters for an inexpensive price contributes to their rise in popularity. Then ultimately, we move within the imaging receiver to realize the goals in developing a receiver as having a flat form factor, a broad view, and low aberration. These design goals happen to be largely defined by the optics used within the image sensor.

Chapter 2 introduces the parameters of a microlens that play a dominant role in the imaging receiver. After an algebraic analysis of a microlens on a thick substrate, simulations for realistic scenarios are presented. These simulations lead us to choose an appropriate microlens orientation and shape. They also provide a means of hypothesizing and visualizing the metrics tied to the design goals for each implementation.

Chapter 3 introduces a custom assembled microlens fabrication method made of individual dispensing and actuation sub systems. The purpose of this system is to create

micro-scale lenses with shapes similar in form to those in Chapter 2. The fabrication system implemented is quite flexible in terms of resulting sizes, shapes, materials, etc. For the purpose of this thesis, it is used to make hemispherical microlenses below 1 mm in diameter with varying contact angles.

Chapter 4 shows the integration of the microlens implementations in Chapter 3 with the image sensor to make an imaging receiver. In each case, this receiver is characterized on an indoor OW communication test bench. The OW communication test bench is used for an experimental evaluation of the metrics associated to the design goals of flat form factor, broad view and minimum focal spot size.

Finally, Chapter 5 concludes the thesis by summarizing the work done and the conclusions reached through the hypothesized and experimental comparisons. In addition, suggestions for future work are also given for different technology emerging from this thesis.

## Chapter 2: Analyses of Microlenses

The imaging characteristics of microlenses are analysed in this chapter for their use within imaging receivers. As stated in the previous chapter, there are three metrics that should be generally optimized for the microlens within an imaging receiver used in OW communication systems.

- i. Metric I for the microlens is its focal length. The focal length should be minimized to realize an imaging receiver with a flat form factor.
- ii. Metric II for the microlens is its FOV. The FOV should be maximized to allow the imaging receiver to function with a broad view.
- iii. Metric III for the microlens is its focal spot size. The focal spot size should be minimized to have the imaging receiver capture images with minimum aberration.

The following sections present analyses on the above metrics for the microlens to understand and visualize its parameters and select an appropriate implementation for its use within an imaging receiver. These implementations would have the microlens be on a thick substrate, on a thin substrate, and under a thin substrate.

### 2.1 Analysis of a Microlens on a Thick Substrate

We will start with an analysis of the most basic implementation of a microlens, with it being situated on an infinitely thick substrate. Such a system can be characterized by a simple algebraic analysis. The algebraic analysis is then verified through a ray-tracing analysis simulation. The plano-convex microlens is assumed to have a spherical profile for its curved surface. It has a refractive index of  $n$ , diameter of  $d$ , radius of curvature of  $R$ , contact angle of

$\alpha$  around its perimeter, and sag of  $s$ . (The sag is the thickness of the microlens along the central optical axis (OA).) The substrate also has a refractive index of  $n$ . The parameters are displayed in the cross-sectional profile shown in Figure 2.1. The figure also shows  $x$ - and  $z$ -coordinates for directions perpendicular and parallel to the OA, respectively.

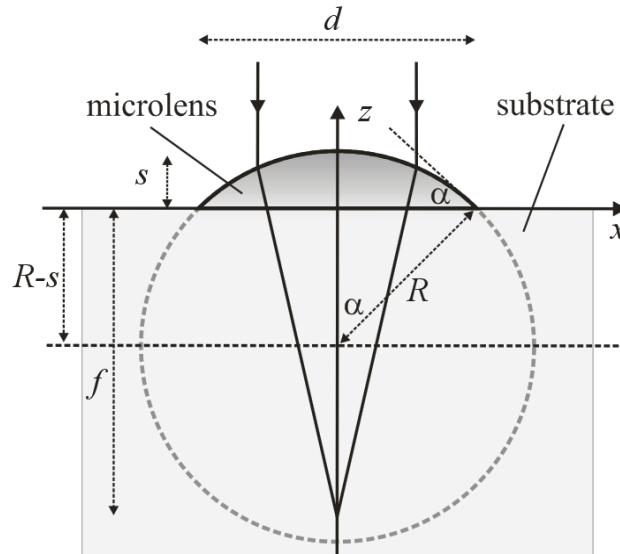


**Figure 2.1** Cross-sectional profile of a microlens on a thick substrate. It has a diameter of  $d$ , radius of curvature of  $R$ , contact angle of  $\alpha$  around its perimeter, and sag of  $s$ , being the thickness of the microlens on the OA. The microlens and substrate both have a refractive index of  $n$ . The coordinates  $(x,z)$  are defined with respect to an origin at the intersection of the planar surface and the OA. Two light rays run parallel to the OA at the top of the figure and intersect the OA at the focal point. The distance along the OA from the origin to the focal point is the focal length,  $f$ .

The curved surface of the microlens is defined by the equation  $x^2 + (z + (R - s))^2 = R^2$ , where  $0 \leq z \leq s$ . The point at the outermost edge of the curved surface, being  $(x,z) = (d/2,0)$ , establishes the relationship

$$R = \frac{s}{2} + \frac{(d/2)^2}{2s}. \quad (1)$$

It is also apparent, by way of the geometry in the figure, that the contact angle is defined by

$$\tan \alpha = \frac{d/2}{R-s} = \frac{4(s/d)}{1-4(s/d)^2}, \quad (2)$$

where the second equality is formed by substituting in the expression for  $R$  from (1). Equation (2) can be solved via the quadratic formula, for the one physical root, to define a normalized sag with respect to the diameter,  $s/d$ , in terms of the contact angle,  $\alpha$ . This gives

$$s/d = \frac{\tan \alpha}{2(1+\sec \alpha)}. \quad (3)$$

In the limit of small contact angles, as  $\alpha$  approaches 0 in (3), we get  $\tan \alpha \approx \alpha$  in the numerator and  $2(1+\sec \alpha) \approx 4$  in the denominator. This gives a normalized sag of  $s/d \approx \alpha/4$  for small  $\alpha$ . In the limit of large contact angles, as  $\alpha$  approaches  $\pi/2$  in (3), the right hand side of the equation becomes indeterminate, with an infinity-over-infinity form, and L'Hôpital's rule is applied. This gives a normalized sag of  $s/d \approx 1/2$  for large  $\alpha$ . This result makes sense from a geometrical standpoint, because the sag becomes equal to the radius of the microlens when the contact angle is  $\pi/2$ .

To define the imaging characteristics of the microlens, in terms of its physical parameters, we consider the focal length (Metric I). We will do this by defining the normalized focal length as the focal length,  $f(\alpha)$ , being the distance along the  $z$ -axis from the origin to the point at which incident light rays running parallel to the OA intersect, normalized with respect to the microlens diameter,  $d$ . This normalized focal length,  $f(\alpha)/d$ , is equivalent to the term 'f-number' that is often seen in the literature [17], and it is considered in this work because the other dimensions in the analysis are normalized with respect to  $d$ . Such normalization allows all the results to be scaled in proportion to the microlens diameter. The normalized focal

length can be linked to the radius of curvature,  $R(\alpha)$ , via the lens maker's formula, which gives  $f(\alpha)/d = R(\alpha)/((n-1)d)$ , where the radius of curvature is a function of the contact angle,  $\alpha$ , and  $n$  is the refractive index of the microlens and substrate. With the above definitions, and (1), the normalized focal length can be expressed as

$$f(\alpha)/d = \frac{R(\alpha)/d}{n-1} = \frac{s/d}{2(n-1)} + \frac{1}{8(s/d)(n-1)} = \frac{\tan \alpha}{4(n-1)(1+\sec \alpha)} + \frac{1+\sec \alpha}{4(n-1)\tan \alpha}. \quad (4)$$

In the limit of small contact angles, as  $\alpha$  approaches 0 and  $s/d$  approaches  $\alpha/4$ , the second terms in (4) dominate over the first terms, giving a normalized focal length of  $f(\alpha \ll \pi/2)/d \approx 1/(\alpha(n-1))$ . For a refractive index of  $n = 1.5$ , roughly corresponding to that of glass and polymer, this gives  $f(\alpha \ll \pi/2)/d \approx 2/\alpha$ . In the limit of large contact angles, as  $\alpha$  approaches  $\pi/2$  and  $s/d$  approaches  $1/2$ , (4) can be evaluated directly with  $s/d = 1/2$ , giving  $f(\alpha \approx \pi/2)/d \approx 1/(2(n-1))$ . For a refractive index of  $n = 1.5$ , this gives  $f(\alpha \approx \pi/2)/d \approx 1$ .

To further define the imaging characteristics of a microlens, in terms of its physical parameters, we next consider the FOV (Metric II). The term FOV that is used in this work refers to an angle, and is equivalent to the term 'angular FOV' seen in literature, and thus it has units of degrees or radians as appropriate. This is in contrast to alternative definitions for FOV that quantify solid angle or area. The FOV of the microlens that is considered here is defined as twice the incident polar angle at which the chief ray, running along the centre of the incident beam, strikes the perimeter of the microlens. Using this definition, and the result for  $f(\alpha)/d$  in (4), the expression for the FOV is

$$\text{FOV}(\alpha) = 2 \arctan \left( \frac{d}{2f(\alpha)} \right) = 2 \arctan \left( \frac{2(n-1)\tan \alpha(1+\sec \alpha)}{\tan^2 \alpha + (1+\sec \alpha)^2} \right) = 2 \arctan((n-1)\sin \alpha). \quad (5)$$

In the limit of small contact angles, as  $\alpha$  approaches 0, (5) gives  $\text{FOV}(\alpha \ll 90^\circ) \approx 2\arctan((n-1)\alpha)$ . For a refractive index of  $n = 1.5$ ,  $\text{FOV}(\alpha \ll 90^\circ) \approx 2\arctan(\alpha/2) \approx \alpha$ . In the limit of large contact angles, as  $\alpha$  approaches  $90^\circ$ , (5) gives  $\text{FOV}(\alpha \approx 90^\circ) \approx 2\arctan(n-1)$ . For a refractive index of  $n = 1.5$ ,  $\text{FOV}(\alpha \approx 90^\circ) \approx 2\arctan(1/2) \approx 0.927 \text{ rad} \approx 53.13^\circ$ .

These results, from the algebraic analyses, can be confirmed through a ray-tracing simulation. The ray-tracing analysis is carried out via RayOptik software. The simulations project a dense grid of rays at the cylindrically-symmetric microlens in three-dimensional space. The rays are focused by the microlens and intersect below the substrate at the focal point. The distance between the top surface of the substrate and the focal point is defined as the focal length,  $f$ . As points of comparison, the following figures show simulation results for a low-contact-angle (LCA) microlens with a contact angle of  $\alpha = 30^\circ$  and a high-contact-angle (HCA) microlens with a contact angle of  $\alpha = 90^\circ$ . Figure 2.2 (a) and (b) show ray-tracing simulations for the LCA microlens with a contact angle of  $\alpha = 30^\circ$ . It has a normalized radius of curvature of  $R/d = 1$  and normalized sag of  $s/d = 0.134$ . The microlens is situated on top of a infinitely thick substrate. These two ray tracing results clearly illustrate the first two metrics of the focal length and FOV. In Figure 2.2(a), the focal length can be seen as the point where the refracted incident rays converge. Figure 2.2(b) shows the max

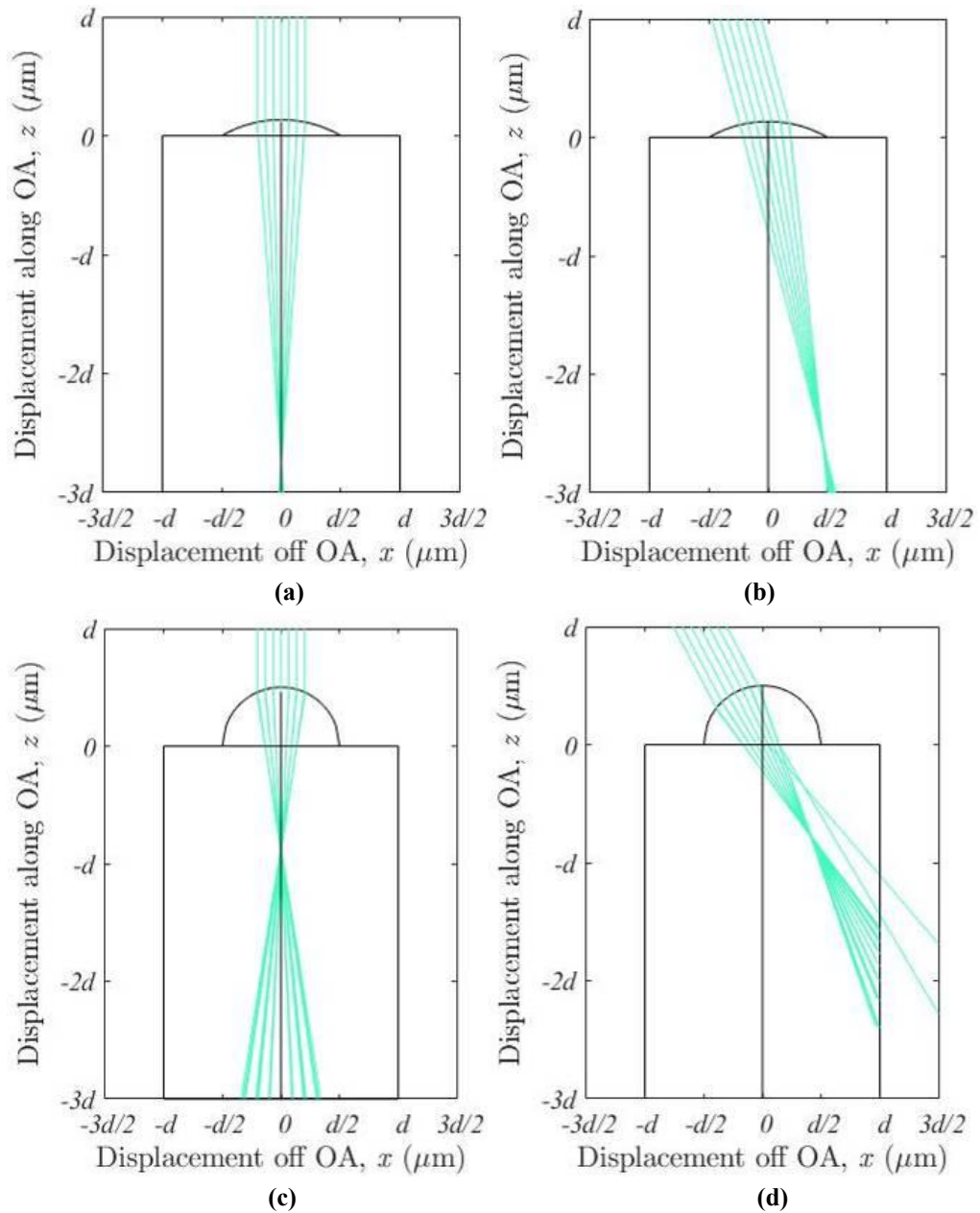
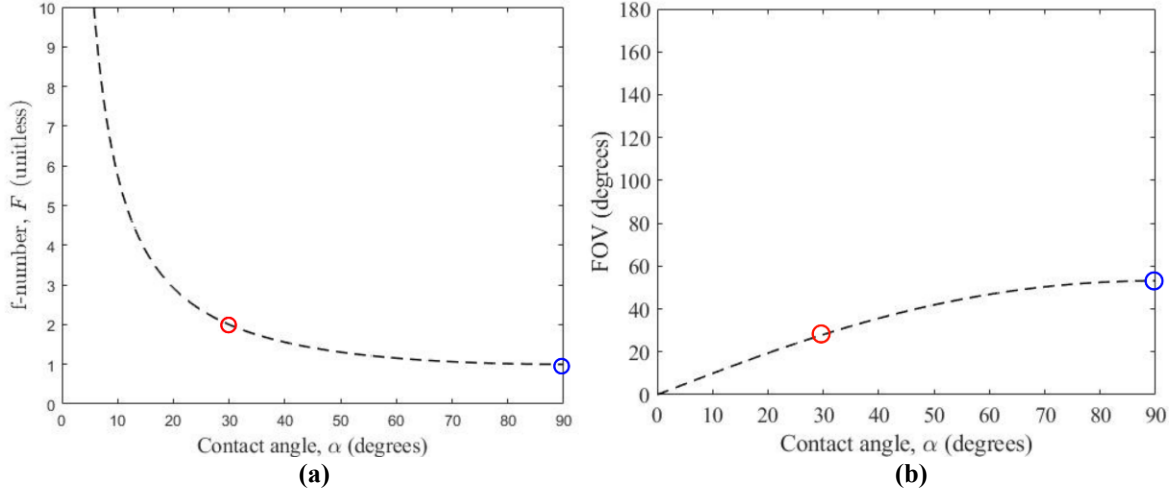


Figure 2.2 Ray-tracing simulations of microlenses with a diameter of  $d$  on an infinitely thick substrate, where the microlens and substrate both have a refractive index of  $n = 1.5$ . The system is shown for the (a) LCA microlens with a contact angle of  $\alpha = 30^\circ$  and rays at an incident polar angle of  $\theta = 0^\circ$ , (b) LCA microlens with a contact angle of  $\alpha = 30^\circ$  and rays at an incident polar angle of  $\theta = 16^\circ$ , (c) HCA microlens with a contact angle of  $\alpha = 90^\circ$  and rays at an incident polar angle of  $\theta = 0^\circ$ , and (d) HCA microlens with a contact angle of  $\alpha = 90^\circ$  and rays at an incident polar angle of  $\theta = 28.5^\circ$ .

FOV by showing the maximum possible incident angle so that focusing occurs on the focal plane below the microlens. Figure 2.2(c) and (d) show the same scenario with a high contact angle microlens.

The trend of the simulation results in Figure 2.2 agree with the results from the algebraic analysis. In the algebraic analysis, it was predicted that a LCA microlens should have a normalized focal length of  $f(\alpha \ll \pi/2)/d \approx 2/\alpha$  and the HCA should be  $f(\alpha \approx \pi/2)/d \approx 1$ . These results can be confirmed for the LCA and HCA microlenses, respectively, in Figure 2.2(a) and (c). In Figure 2.2(a), where  $\alpha = 30^\circ$ , the algebraic analysis predicts the normalized focal length to be  $f(\alpha=30^\circ)/d \approx 3.82$ , and the ray-tracing analysis shows  $f(\alpha=30)/d = 2.75$ . Likewise, in Figure 2.2(c), the algebraic analysis predicts the normalized focal length to be  $f(\alpha \approx \pi/2)/d \approx 1$ , and the ray-tracing analysis shows  $f(\alpha=90)/d = 0.9$ .

The general imaging characteristics from Equation (4) and (5) of the microlens on a thick substrate are shown in Figure 2.3 for all contact angles. Figure 2.3(a) shows the metric of normalized focal length,  $f(\alpha)/d$ , as a function of the contact angle,  $\alpha$ . As explained earlier, we see the normalized focal length transition from a hyperbola for small contact angles,  $f(\alpha \ll 90^\circ)/d \approx 2/\alpha$ , to a constant for large contact angles,  $f(\alpha \approx 90^\circ)/d \approx 1$ . Figure 2.3(b) shows the metric of FOV as a function of the contact angle,  $\alpha$ . This also agrees with the results from earlier, with the FOV transitioning from a linear trend for small contact angles,  $\text{FOV}(\alpha \ll 90^\circ) \approx 2\arctan(\alpha/2) \approx \alpha$ , to a constant for large contact angles,  $\text{FOV}(\alpha \approx 90^\circ) \approx 0.927 \text{ rad} \approx 53.13^\circ$ . According to Figures 2.3(a) and (b), the contact angle of a microlens can be increased to minimize the focal length (Metric I) and maximize the FOV (Metric II).



**Figure 2.3 Imaging characteristics of a microlens on a thick substrate showing the (a) normalized focal length,  $f/d$ , and (b) FOV versus the contact angle,  $\alpha$ . For an increasing contact angle in (a), the normalized focal length transitions from a hyperbola,  $f(\alpha \ll 90^\circ)/d \approx 2/\alpha$ , to a constant of  $f(\alpha \approx 90^\circ)/d \approx 1$ . For increasing contact angle in (b), the FOV transitions from a linear trend,  $\text{FOV}(\alpha \ll 90^\circ) \approx \alpha$ , to a constant of  $\text{FOV}(\alpha \approx 90^\circ) \approx 53.13^\circ$ . Data points for the LCA microlens with  $\alpha = 30^\circ$  and the HCA microlens with  $\alpha = 90^\circ$  are enclosed by red and blue circles, respectively.**

To proceed, we must recognize that there were oversights made in this analysis of the microlens. First, the microlens was assumed to be on an infinitely thick substrate, with the resulting image plane being buried within the substrate. Such a scenario is an idealization, because it would require the image sensor to be embedded within the substrate. Second, the focal length was estimated by the lens maker's formula. As such, the result of the algebraic analysis did not match the ray-tracing simulation, although the results have similar trends. Lastly, the third metric for focal spot size was ignored during the algebraic and ray-tracing simulation analyses of the microlens on a substrate of infinite thickness. The work presented in the next section removes these idealities by using a substrate with a finite thickness.

## 2.2 Analysis of a Microlens on a Thin Substrate

The characterization of a microlens on a thin substrate makes use of the ray-tracing analysis. Such an approach allows for the investigation of complex optical systems with features that are much larger than the wavelength, as is the case here. A cross-sectional profile of the microlens on a thin substrate is shown in Figure 2.4. The figure has the same dimensions and labels as those for the thick substrate, albeit with a substrate having a thickness of  $t$ . It is worthwhile to note that the displayed light rays refract inward slightly at the lower glass-air interface, and this can further reduce the normalized focal length. In this section, the third metric can now be assessed by simulating the spot size of the focal spot on the image sensor.

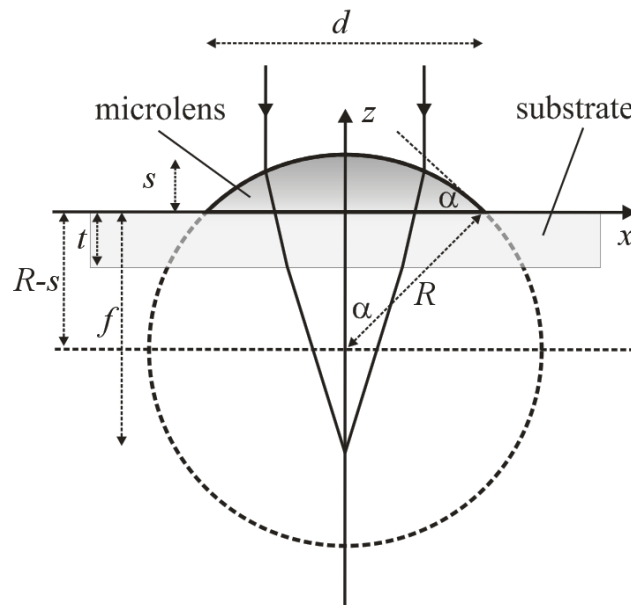


**Figure 2.4** Cross-sectional profile of a microlens on a thin substrate. The microlens has a diameter of  $d$ , radius of curvature of  $R$ , contact angle of  $\alpha$  around its perimeter, and sag of  $s$ , being the thickness of the microlens on the OA. The substrate has a thickness of  $t$ . The microlens and substrate both have a refractive index of  $n$ . The coordinates  $(x,z)$  are defined with respect to an origin at the intersection of the top planar surface and the OA. Two light rays run parallel to the OA at the top of the figure and intersect the OA at the focal point. The distance from the origin to the focal point is the focal length,  $f$ .

Representative simulations for the microlens on the thin substrate are shown in Figure 2.5. As an inset in Figure 2.5, the resultant image of a screen at the focal plane is shown to illustrate the focal spot size. Figures 2.5(a) and (b) show ray-tracing simulations for the LCA microlens with a contact angle of  $\alpha = 30^\circ$ . It has a normalized radius of curvature of  $R/d = 1$  and normalized sag of  $s/d = 0.134$ . The microlens is situated on top of a substrate with a normalized thickness of  $t/d = 0.2$ . Figure 2.5(a) shows a ray-tracing simulation for incident rays being parallel to the OA with an incident polar angle of  $\theta = 0^\circ$ . The normalized focal length seen here is  $f/d = 1.91$ . Figure 2.5(b) shows a ray-tracing simulation for incident rays being oblique to the OA, with an incident polar angle of  $\theta = 14.2^\circ$ . For this angle, the chief ray of the incident beam strikes the outermost edge of the allowed imaging area on the image sensor, being directly below the outermost edge of the microlens. Thus, this case defines the largest allowed incident polar angle and sets the FOV of this microlens at  $2 \times 14.2^\circ = 28.4^\circ$ .

Figures 2.5(c) and (d) show ray-tracing simulations for the HCA microlens with a contact angle of  $\alpha = 90^\circ$ . It has a normalized radius of curvature of  $R/d = 0.5$  and normalized sag of  $s/d = 0.5$ . It is situated on top of a substrate with a normalized thickness of  $t/d = 0.2$ . Figure 2.4(c) shows results for incident rays that are parallel to the OA with an incident polar angle of  $\theta = 0^\circ$ . The normalized focal length seen here is  $f/d = 0.68$ . Figure 2.5(d) shows a simulation for incident rays that are oblique to the OA, with an incident polar angle of  $21.5^\circ$ . Again, the chief ray strikes the outermost edge of the allowed imaging area on the image sensor, being directly below the outermost edge of the microlens. This case defines the largest allowed polar angle and sets the FOV of this microlens at  $2 \times 21.5 = 43.0^\circ$ .

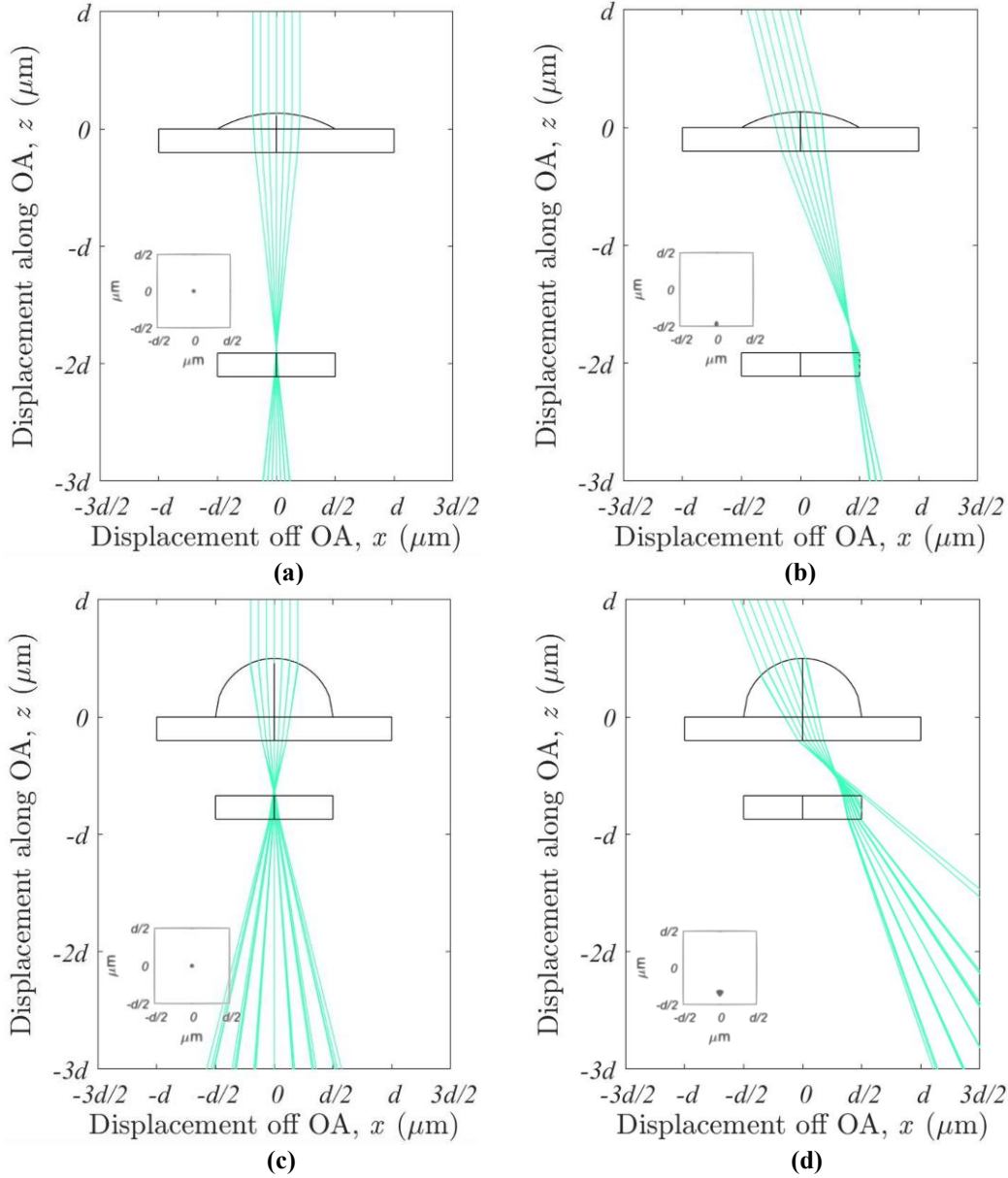


**Figure 2.5** Ray-tracing simulations of microlenses with a diameter of  $d$  on a thin substrate with a normalized thickness of  $t/d = 0.2$ , where the microlens and substrate both have a refractive index of  $n = 1.5$ . The system is shown for the (a) LCA microlens with a contact angle of  $\alpha = 30^\circ$  and rays at an incident polar angle of  $\theta = 0^\circ$ , (b) LCA microlens with a contact angle of  $\alpha = 30^\circ$  and rays at an incident polar angle of  $\theta = 14.2^\circ$ , (c) HCA microlens with a contact angle of  $\alpha = 90^\circ$  and rays at an incident polar angle of  $\theta = 0^\circ$ , and (d) HCA microlens with a contact angle of  $\alpha = 90^\circ$  and rays at an incident polar angle of  $\theta = 21.5^\circ$ .

The impact of the finite substrate thickness in the figures is two-fold. First, the finite substrate thickness allows for a smaller normalized focal length,  $f/d$ , because the substrate's lower glass-air interface refracts light inward and reduces the focal length. Second, the finite substrate thickness reduces the FOV from  $53.13^\circ$  to  $43.0^\circ$ . This comes about because the lower glass-air interface refracts the chief ray away from the OA.

The impact of the contact angle is that the HCA allows for a smaller normalized focal length (Metric I) and a higher FOV (Metric II), as seen before, however to complete the analyses of the microlens on a thin substrate, it is necessary to consider the focal spot size (Metric III). The focal spot for the HCA microlens at an incident polar angle of  $\theta = 0^\circ$ , seen in Figure 2.5(c), is larger than that for the LCA microlens at an incident polar angle of  $\theta = 0^\circ$ , seen in Figure 2.5(a). This is due to the increased presence of spherical aberration for the HCA microlens. Spherical aberration has light rays at the perimeter of the incident beam focus earlier than the more centralized rays, which results in poorly defined and larger focal spots for the HCA microlens. It should also be noted that the focal spot for the HCA microlens at an incident polar angle of  $\theta = 21.5^\circ$ , seen in Figure 2.5(d), is larger than that for the LCA microlens at an incident polar angle of  $\theta = 13.0^\circ$ , seen in Figure 2.5(b). This is due to flaring of the focal spot in the former figure. Flaring manifests itself as an asymmetric focal spot in the image plane with a high density of rays close to the OA and a low density of rays far from the OA. Thus, the focal spot in the transverse image plane resembles a comet—with a highest intensity focal spot close to the OA and a low-intensity tail flaring away from the OA. It is because of the resemblance to a comet that the effect is referred to as comatic aberration. Note that having the microlens situated on a substrate with a finite thickness worsens the comatic aberration. It can be seen in Figure 2.5(d), that incident rays closest to

the OA preferentially refract towards the OA as they exit the lower glass-air interface, while incident rays furthest from the OA preferentially refract away from the OA as they exit the lower glass-air interface. Both spherical and comatic aberration are undesirable because they lead to larger focal spot sizes, which spreads the signal power over a greater number of pixels on the image sensor and makes it difficult to distinguish the signal intensity from the background intensity. For this reason, the focal spot size (Metric III) is considered next. For more detail on the types of aberration and the distorted effect they have on the focal spot see Appendix A.

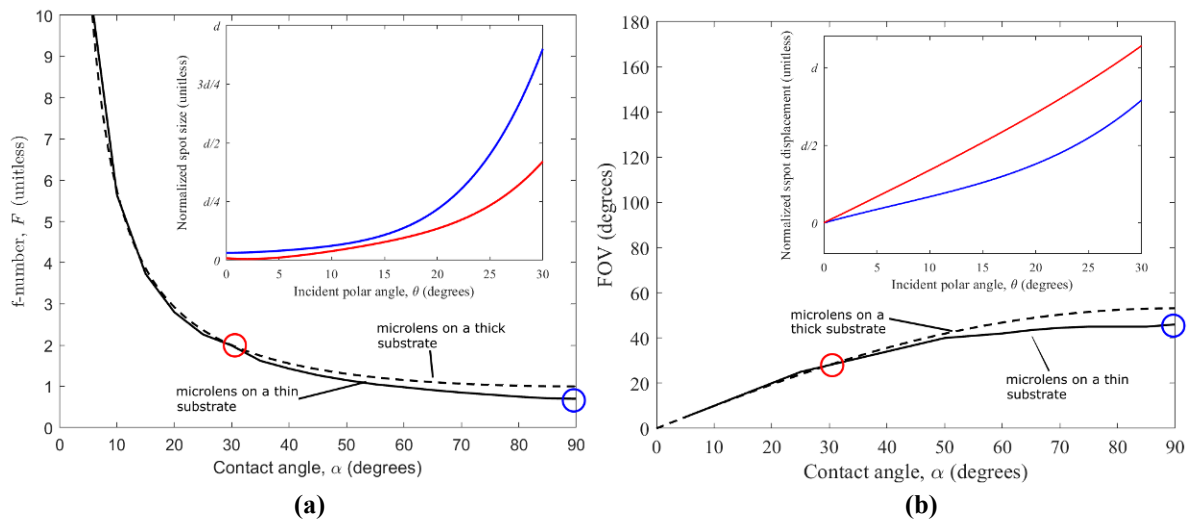


**Figure 2.6** Imaging characteristics of a microlens on a thin substrate showing the (a) normalized focal length,  $f/d$ , and (b) FOV versus the contact angle,  $\alpha$ , given a microlens with a diameter of  $d$ , a substrate with a normalized thickness of  $t/d = 0.2$ , and a refractive index of  $n = 1.5$ . The prior results for a microlens on a thick substrate are also shown. According to (a) and (b), an increasing contact angle yields a shorter normalized focal length and a wider FOV. Data points for the LCA microlens with  $\alpha = 30^\circ$  and the HCA microlens with  $\alpha = 90^\circ$  are enclosed by red and blue circles, respectively.

A series of ray-tracing simulations were performed to obtain the focal spot size as a function of the incident polar angle,  $\theta$ , and the results are shown in the insets of Figure 2.6 with separate curves for the LCA microlens with a contact angle of  $\alpha = 30^\circ$  and the HCA microlens with a contact angle of  $\alpha = 90^\circ$ . Figure 2.6(a) inset shows the normalized focal spot displacement versus the incident polar angle,  $\theta$ . This quantity is the displacement of the chief ray from the OA normalized with respect to the microlens diameter,  $d$ .

Note that the definition for the FOV, as twice the incident polar angle for the case of a chief ray striking the perimeter of the microlens, corresponds to a value of  $d/2$  on the vertical axis. Thus, the intersections of the two curves with respect to a horizontal line of 0.5 define incident polar angles that are one-half of the FOV. Thus, this figure shows that the FOVs of the LCA and HCA microlens are  $2 \times 14.2^\circ = 28.4^\circ$  and  $2 \times 21.5^\circ = 43.0^\circ$ , respectively, which agree closely with the results of Figure 2.5(b) and (d). The Figure 2.6(a) inset shows the normalized focal spot size versus the polar angle,  $\theta$ , for the LCA and HCA microlenses. The focal spot size is defined here by calculating the area of the focal spot on the image sensor, as the area in which the intensity is at or above half the peak intensity, and dividing this result by  $\pi$ , taking the square root, and multiplying the result by 2. In this way, the normalized focal spot size can be visualized as an effective diameter of the focal spot normalized with respect to the microlens diameter.

The results in Figure 2.6(b) show that the normalized focal spot size of the HCA microlens at small incident polar angles, being  $\sim 1/32$ , is greater than that of the LCA microlens, being  $\sim 1/64$ . This is a manifestation of the greater spherical aberration for the HCA microlens that was commented upon earlier. The results in the inset of Figure 2.6(b) also show that the normalized spot size of the HCA microlens grows to  $\sim 1/2$  at an incident

polar angle of  $20^\circ$ , which is greater than the corresponding normalized spot size of  $\sim 1/4$  for the LCA microlens. This is a manifestation of the greater comatic aberration for the HCA microlens that was commented upon earlier.

### 2.3 Analysis of a Microlens under a Thin Substrate

It became clear in the prior section that a microlens with a larger contact angle could yield a shorter focal length and a wider FOV. However, it was also found that these gains came at the expense of having larger aberration and a bigger focal spot size. Given the conflict in these metrics, this section considers an implementation with the microlens being under a thin substrate. Such an implementation eliminates the refraction at the lower glass-air interface that was seen in the prior section to promote comatic aberration. The new implementation is shown as a cross-sectional profile in Figure 2.7. Its definitions are similar to those of Figure 2.3, but in this case the microlens and substrate are flipped vertically.

Figures 2.8(a) and (b) show ray-tracing simulations for the LCA microlens with a contact angle of  $\alpha = 30^\circ$ . It has a normalized radius of curvature of  $R/d = 1$  and normalized sag of  $s/d = 0.134$ . The microlens is situated under a substrate with a normalized thickness of  $t/d = 0.2$ . The microlens and substrate both have a refractive index of  $n = 1.5$ . Figure 2.8(a) shows a ray-tracing simulation for incident rays being parallel to the OA with an incident polar angle of  $\theta = 0^\circ$ . The normalized focal length is seen here to be  $f/d = 2.05$ . Figure 2.8(b) shows a ray-tracing simulation for incident rays being oblique to the OA with an incident polar angle of  $\theta = 13.0^\circ$ . For this angle, the chief ray of the incident beam strikes the outermost edge of the allowed imaging area on the image sensor, being directly below the outermost edge of the microlens. Thus, this simulation corresponds to the largest allowed incident polar angle and sets the FOV of this microlens at  $2 \times 13.0^\circ = 26.0^\circ$ .

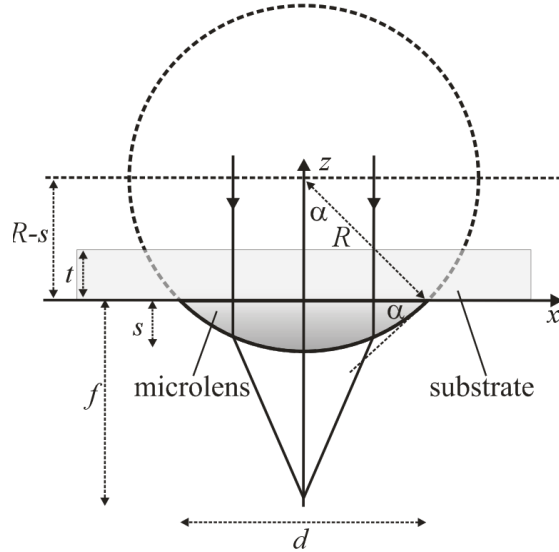


**Figure 2.7** Cross-sectional profile of a microlens under a thin substrate. The microlens has a diameter of  $d$ , radius of curvature of  $R$ , contact angle of  $\alpha$  around its perimeter, and sag of  $s$ , being the thickness of the microlens on the OA. The substrate has a thickness of  $t$ . The microlens and substrate both have a refractive index of  $n$ . The coordinates  $(x,z)$  are defined with respect to an origin at the intersection of the bottom planar surface and the OA. Two light rays run parallel to the OA at the top of the figure and intersect the OA at the focal point. The distance from the origin to the focal point is the focal length,  $f$ .

Figures 2.8(c) and (d) show ray-tracing simulations for the HCA microlens with a contact angle of  $\alpha = 90^\circ$ . It has a normalized radius of curvature of  $R/d = 0.5$  and normalized sag of  $s/d = 0.5$ . It is situated under a substrate with a normalized thickness of  $t/d = 0.2$ . The microlens and substrate both have a refractive index of  $n = 1.5$ . Figure 2.8(c) shows results for incident rays that are parallel to the OA, with an incident polar angle of  $\theta = 0^\circ$ . The normalized focal length is seen here to be  $fd = 1.41$ . Figure 2.4(d) shows a simulation for incident rays that are oblique to the OA with an incident polar angle of  $28.0^\circ$ . Again, the chief ray strikes the outermost edge of the allowed imaging area on the image sensor, being directly below the outermost edge of the microlens. This simulation corresponds to the largest allowed polar angle and sets the FOV of this microlens at  $2 \times 28.0 = 56.0^\circ$ .

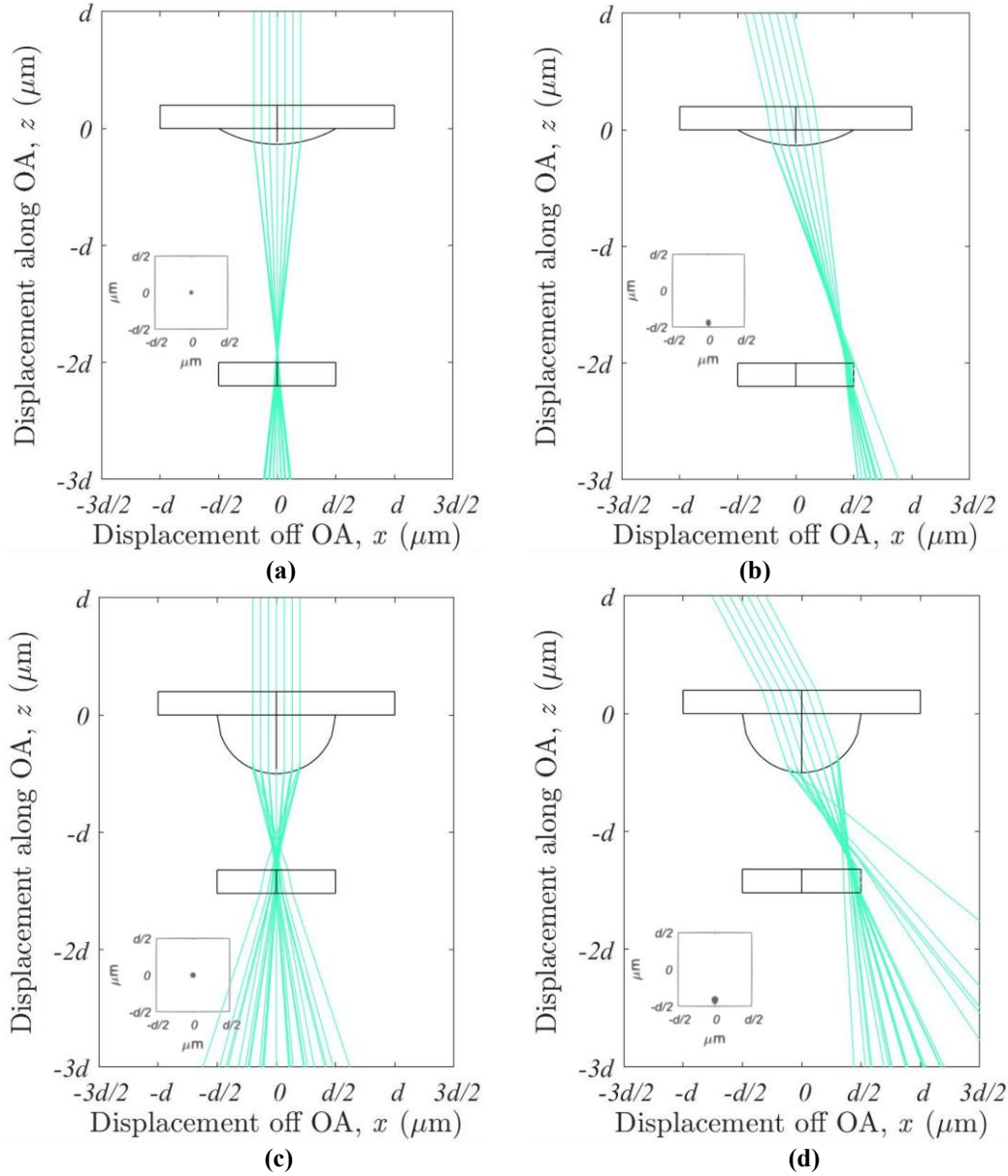


**Figure 2.8** Ray-tracing simulations of microlenses with a diameter of  $d$  under a thin substrate with a normalized thickness of  $t/d = 0.2$ , where the microlens and substrate both have a refractive index of  $n = 1.5$ . The system is shown for the (a) LCA microlens with a contact angle of  $\alpha = 30^\circ$  and rays at an incident polar angle of  $\theta = 0^\circ$ , (b) LCA microlens with a contact angle of  $\alpha = 30^\circ$  and rays at an incident polar angle of  $\theta = 13^\circ$ , (c) HCA microlens with a contact angle of  $\alpha = 90^\circ$  and rays at an incident polar angle of  $\theta = 0^\circ$ , and (d) HCA microlens with a contact angle of  $\alpha = 90^\circ$  and rays at an incident polar angle of  $\theta = 26^\circ$ .

The general trends for the normalized focal length,  $f/d$ , and FOV of the microlens under a thin substrate are shown in Figures 2.9(a) and (b), respectively, as a function of the contact angle,  $\alpha$ , for a refractive index of  $n = 1.5$ . For comparison, the figures also show the prior results for the microlens on a thick substrate. Recall the microlens on a thin substrate had a FOV slightly below the microlens on the thick substrate. In this case we are seeing the FOV slightly above that of the microlens on a thick substrate.

The impact seen here of having the microlens be under the substrate is two-fold. First, as seen in Figure 2.9(a), it increases the normalized focal length and the extent to which the length is increased grows with the contact angle. Having the LCA microlens on and under the substrate gives similar normalized focal lengths of  $f/d = 1.91$  and  $2.05$ , respectively, while having the HCA microlens on and under the substrate gives distinct normalized focal lengths of  $f/d = 0.68$  and  $1.41$ , respectively. Second, as seen in Figure 2.9(b), having the microlens under the substrate is seen to increase the FOV and the extent to which it increases grows with the contact angle. Having the LCA microlens on and under the substrate gives similar FOVs of  $28.0^\circ$  and  $26.0^\circ$ , respectively, while having the HCA microlens on and under the substrate gives FOVs of  $43.0^\circ$  and  $56.0^\circ$ , respectively. Here, situating the microlens under rather than on the substrate has eliminated refraction at the lower glass-air interface, which lessens the FOV because it refracts the exiting rays away from the OA, and has introduced refraction at the upper air-glass interface, which augments the FOV because it refracts the incident rays towards the OA. Overall, it can be seen that situating the microlens under rather than on the substrate increases the focal length (in opposition to Metric I) increases the FOV (in support of Metric II). For this reason, the focal spot size (being Metric III) is considered next for these implementations.

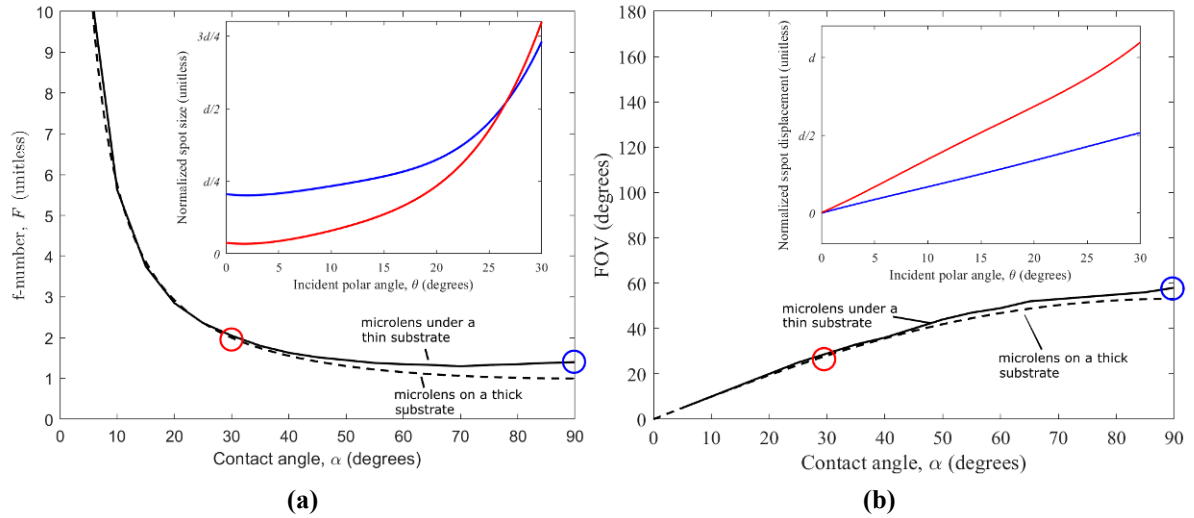


**Figure 2.9** Imaging characteristics of a microlens under a thin substrate showing the (a) normalized focal length,  $f/d$ , and (b) FOV versus the contact angle,  $\alpha$ , given a microlens with a diameter of  $d$ , a substrate with a normalized thickness of  $t/d = 0.2$ , and a refractive index of  $n = 1.5$ . The prior results for a microlens on a thick substrate and a microlens on a thin substrate are also shown. According to (a) and (b), an increasing contact angle yields a shorter normalized focal length and a wider FOV. Data points for the LCA microlens with  $\alpha = 30^\circ$  and HCA microlens with  $\alpha = 90^\circ$  are enclosed by red and blue circles, respectively.

A series of ray-tracing simulations were performed to analyse the focal spot as a function of the incident polar angle,  $\theta$ , and the results are shown in the insets of Figure 2.9 with separate curves for the LCA microlens with a contact angle of  $\alpha = 30^\circ$  and the HCA microlens with a contact angle of  $\alpha = 90^\circ$ . The substrate thickness is  $t = 0.2d$  and the refractive index is  $n = 1.5$ . Figure 2.9(a) shows the normalized focal spot displacement versus the polar angle,  $\theta$ . As before, the displacement is that of the chief ray from the OA normalized with respect to the microlens diameter,  $d$ , and the intersections of the two curves with a horizontal line at 0.5 denotes one-half of the FOV. It can be seen from this figure that the FOV of the HCA microlens, at  $2 \times 28.0^\circ = 56.0^\circ$ , is wider than that of the LCA microlens,

at  $2 \times 13.0^\circ = 26.0^\circ$ . Such findings agree with the results and conclusions of Figure 2.9(b). Figure 2.9(b) inset shows the normalized focal spot size versus the polar angle,  $\theta$ . As before, the focal spot size is defined here as an effective diameter of the focal spot normalized with respect to the microlens diameter. The results in this figure show that the normalized focal spot size of the HCA microlens at small incident polar angles, being  $\sim 1/16$  is greater than that of the LCA microlens, being  $\sim 1/32$ . This is a manifestation of the greater spherical aberration for the HCA microlens that was commented upon earlier. The results in the inset of Figure 2.9(b) also show that the normalized spot size of the HCA microlens grows to  $\sim 2/5$  at an incident polar angle of  $20^\circ$ , which is less than the corresponding normalized spot size of  $\sim 1/4$  for the LCA microlens. Moreover, the normalized spot size of the HCA microlens seen here is less than the corresponding value of  $\sim 1/2$  for the HCA microlens on a thin substrate in Figure 2.6(b). Thus, having the HCA microlens be under the thin substrate has reduced the comatic aberration and the focal spot size, as predicted.

## 2.4 Discussion

The findings from the prior sections identify means by which the focal length (Metric I) can be decreased, the FOV (Metric II) can be increased, and the focal spot size (Metric III) can be decreased. To this end, we note that the focal length and focal spot size both scale in proportion to the microlens diameter,  $d$ , given that all dimensions in the prior analyses are normalized with respect to  $d$ . We also note that the FOV scales roughly in proportion to the reciprocal of  $f/d$ . This is seen in Figures 2.5 and 2.9 at small contact angles, as the normalized focal length is roughly equal to the reciprocal of the contact angle (in radians) and the FOV is roughly equal to the contact angle. Thus, we have  $\text{FOV} \approx \alpha \approx (f/d)^{-1}$  for small  $\alpha$ .

The stated scaling suggests that the focal length and focal spot size can be decreased by simply reducing the microlens diameter,  $d$ , while the FOV can be widened by increasing the contact angle,  $\alpha$ . Of these two means, increasing the contact angle is arguably more difficult, because the contact angle for standard microlens fabrication techniques, such as thermal reflow [18], is dictated by the materials used via their balancing of surface tension. The diameter, in contrast, can be reduced by simply decreasing the volume of the microlens.

Given the above reasoning, and the fact that the implementation with the microlens under a thin substrate gives the greatest FOV, the work that follows will situate microlenses under a thin substrate. Three microlens implementations will then be investigated and compared:

- i. An LCA microlens will be investigated as a nominal implementation with its results used as a benchmark;
- ii. An HCA microlens will be investigated as an implementation with the potential to realize a wide FOV;
- iii. An LCA microlens array will be investigated as an implementation with the potential to realize a short focal length and small focal spot size.

The latter microlens implementation takes the form of an array because a reduction in the diameter of a microlens must be compensated for by having more microlenses. This is because each implementation must capture the same incident optical power to yield the same signal level. Thus, a microlens array with  $N$  microlenses would need each microlens to have a diameter of  $1/N^{1/2}$  times the diameter of a stand alone microlens.

Table 2.1 shows the characteristics of the three microlens implementations that will be investigated and their metrics from the analyses of this chapter. The table shows the focal length (Metric I), FOV (Metric II), and focal spot size (Metric III) for an LCA microlens,

HCA microlens, and LCA microlens array having  $N = 9$  microlenses, with all of the microlenses being under a thin substrate. The minimal focal length, maximal FOV, and minimal focal spot size are enclosed in boxes. According to the table, it is predicted that the HCA microlens will yield the greatest FOV, while the LCA microlens array will yield the shortest focal length and smallest focal spot size. The following chapters will present the fabrication and testing of these microlens implementations to test these predictions.

**Table 2.1 The focal length, FOV, and focal spot size for the LCA microlens, HCA microlens, and LCA microlens array. The stated focal spot size is the effective diameter of the focal spot at the maximum incident polar angle, i.e., at half the FOV. The microlens diameter,  $d$ , is that of the isolated microlenses.**

	LCA microlens (with $\alpha = 30^\circ$ )	HCA microlens (with $\alpha = 90^\circ$ )	LCA microlens array (with $\alpha = 30^\circ$ )
Metric I, focal length	$2d$	$1.4d$	$\boxed{2d/(9)^{1/2} = 0.67d}$
Metric II, FOV	$28^\circ$	$\boxed{58^\circ}$	$28^\circ$
Metric III, focal spot size*	$0.1d$	$0.7d$	$\boxed{0.1d/9^{1/2} = 0.033d}$

### **Chapter 3: Fabrication of Microlenses**

It was argued earlier within this work that an imaging receiver should have a flat form factor, a broad view of its environment, and minimum aberration. These features can be brought about by combining the image sensor with a microlens with a short focal length, wide FOV, and small focal spot size, respectively. The analyses in the previous chapter suggested that such characteristics could be obtained by controlling the diameter and contact angle of the incorporated microlens. Thus, the microlens fabrication process that is applied should enable careful control of both the diameter and the contact angle of the microlens.

The goal of fabricating a microlens with control of its diameter is fairly straightforward for the conventional thermal reflow process [19]. Thermal reflow is carried out by patterning a solid micron-scale disk out of polymer, typically via photolithography, and then heating the disk. This melts the polymer and surface tensions form the liquid into a roughly spherical shape. The polymer then solidifies into a microlens as it cools. With such a process, it is relatively simple to control the microlens diameter simply patterning smaller or larger disks at the outset.

The goal of fabricating a microlens with control of its contact angle is far from trivial for the conventional thermal reflow process. When this process is carried out with photoresist in air, the shape of the microlens is dictated by the balancing of surface tensions of the polymer, glass substrate, and air. This leads to a relatively low contact angle for conventional polymers on glass substrates. Moreover, the process does not offer a great deal of control of the contact angle because it is difficult to finely tune the discrete surface tensions of the polymer and/or glass.

In any case, it is intuitively easier to control the shape through dispensing polymer than thermal reflow. Due to this reason, other methods have been developed to dispense UV curable polymer lenses [20]. To control the microlens shape, and thus the contact angle, it is necessary to understand the balancing of surface tensions that occurs around the microdroplet before it is solidified. The surface tensions are shown in Figure 3.1. The microdroplet is a liquid (such as polymer) on top of a solid substrate (such as glass) surrounded by an ambient filler (such as air). The solid-filler interfacial energy yields a surface tension that is denoted by  $\gamma_{sf}$ , the solid-liquid interfacial energy yields a surface tension that is denoted by  $\gamma_{sl}$ , and the liquid-filler interfacial energy yields a surface tension that is denoted by  $\gamma_{lf}$ . In equilibrium, the net force per unit length at the three-phase contact line must be zero. This balancing of forces in the figure establishes Young's equation [21], as

$$\gamma_{sf} - \gamma_{sl} - \gamma_{lf} \cos \alpha = 0, \quad (6)$$

which can be manipulated to form an explicit solution for the cosine of the contact angle,

$$\cos \alpha = \frac{\gamma_{sf} - \gamma_{sl}}{\gamma_{lf}}. \quad (7)$$

It is worth noting that the balancing of forces carried out here neglects gravity. This is a good assumption for sufficiently small microdroplets, being on the submillimetre-scale, because such microdroplets have surface tension forces that dominate over body forces like gravity [22].

The challenges of microlens formation for the conventional thermal reflow process are seen explicitly in (7). First, thermal reflow is carried out via heating with air as the surrounding filler. The solid-filler interfacial energy, being on the order of  $\gamma_{sf}(\text{glass-air}) = 310 \text{ mJ/cm}^2$  [23], is far larger than the typical solid-liquid (glass-polymer) interfacial energy,

being on the order of  $\gamma_{sl}(\text{glass-polymer}) = 40 \text{ mJ/cm}^2$ . This yields a large numerator in (7) and a small contact angle. Second, the discrete choices of glass for the substrate and polymer for the microlens leave only coarse control of the contact angle. Thus, it is difficult to finely tune the contact angle.

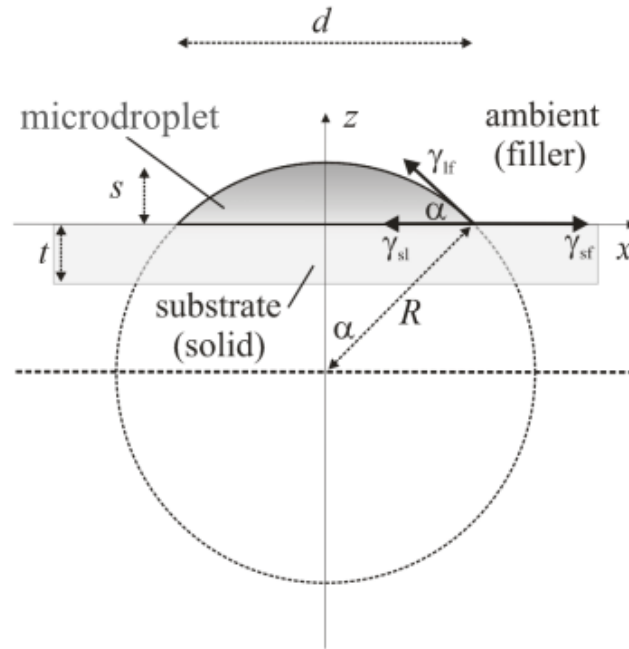


**Figure 3.1** Cross-sectional profile of a representative microdroplet. The liquid microdroplet has a diameter of  $d$ , radius of curvature of  $R$ , contact angle of  $\alpha$  around its perimeter, and sag of  $s$ , being the thickness of the microlens at its centre. The substrate has a thickness of  $t$ . The surrounding medium is an ambient filler. The coordinates  $(x,z)$  are defined with respect to an origin at the intersection of the bottom planar surface and the OA. The three-phase contact line is shown with the solid-filler interfacial energy,  $\gamma_{sf}$ , the solid-liquid interfacial energy,  $\gamma_{sl}$ , and the liquid-filler interfacial energy  $\gamma_{lf}$ .

In this work, an alternative process is used to fabricate microlenses with control of the contact angle. The process makes use of direct dispensing of liquid polymer as a microdroplet on a glass substrate and *in situ* ultraviolet- (UV-) curing of the microdroplet

into a microlens. With this process, it becomes possible to carry out the dispensing and UV-curing in a filler other than air. For example, a filler such as glycerol can be used because it exhibits a lower solid-filler interfacial energy with the glass substrate, making it roughly equal to the solid-liquid interfacial energy  $\gamma_{sl}$ . This increases the contact angle. Moreover, the direct dispensing process allows for direct control and fine tuning of the contact angle via contact angle hysteresis [24]. Contact angle hysteresis comes about from contact line pinning, for which an advancing contact line exhibits an increased contact angle and a receding contact line exhibits a decreased contact angle. In this way, the final contact angle of the microdroplet is a function of the height between the needle tip and substrate when the polymer is dispensed. Thus, this height can be used as a parameter to control the contact angle of the microdroplet. The system that carries out the direct dispensing and UV-curing of the polymer microdroplets into microlenses is described in the following section.

### **3.1 Microlens Fabrication System**

The microlens fabrication system that carries out the direct dispensing and UV-curing of polymer is automated to give precise control of both the dispensing and the curing. The system is shown in Figure 3.2. It is comprised of a control unit (Nordson 7012590), a 30-cc syringe barrel (Nordson 7012143) containing the polymer, with a pneumatically-controlled piston and needle tip (Nordson 7018463), an optical fibre that delivers a UV beam to cure the microdroplet, and an underlying dispensing container. The dispensing container is used to allow for dispensing of microdroplets in the presence of an ambient filler other than air, if desired. It has horizontal dimensions of 28.1 mm  $\times$  28.1 mm and a height of 25 mm to allow for such dispensing onto standard 25.4 mm  $\times$  25.4 mm glass coverslips.

The polymer that is used is Norland Optical Adhesive (NOA) 68. It is chosen for three reasons. First, it has a refractive index of  $n = 1.54$ , which is roughly equal to that of glass. This minimizes potential losses due to reflections at the polymer-glass interface. Second, it is more viscous than other polymers in the NOA series. Its higher viscosity, being approximately 5,000 cps, leads to better control during dispensing. In our experience, less viscous NOA polymers such as NOA 81 flow very easily and this sacrifices reproducibility. Third, NOA 68 has uniform transmissivity across the visible spectrum and near-infrared spectrum, as shown in Figure 3.3. This high transmissivity is useful for broadband operation of imaging receivers. It is also apparent from this figure that the transmissivity of NOA 68 drops, and its absorption increases, significantly at wavelengths below 420 nm. This suggests that the wavelength for curing should be at or below this wavelength. As such, a laser diode with a wavelength of 405 nm is used as the UV-curing source. Photographs of the complete microlens fabrication system are shown in Figure 3.4. Figure 3.4(a) shows the overall microlens fabrication system, including the syringe barrel that is used to dispense the NOA 68 polymer into a microdroplet and the optical fibre that delivers the UV beam to cure the microdroplet. Figure 3.4(b) shows the needle tip in the system that dispenses the polymer in the form of a microdroplet on the glass substrate. The microlens fabrication system is operated via a dispensing sub-system and an actuation sub-system, by way of the LabVIEW interfaces shown in Figure 3.5. The details of these sub-systems are given in the following two subsections.

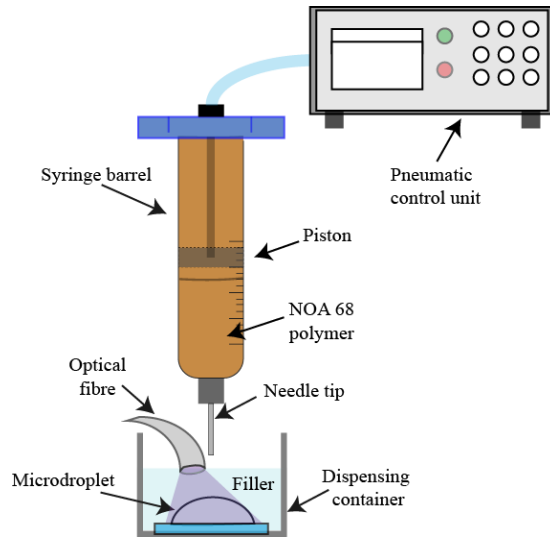


**Figure 3.2** The microlens fabrication system. The system is comprised of a control unit, a syringe barrel containing a piston and the NOA 68 polymer, onto which is attached to the needle tip, and a dispensing container. The dispensing container houses a filler solution, if needed. The microdroplet is dispensed within the dispensing container.

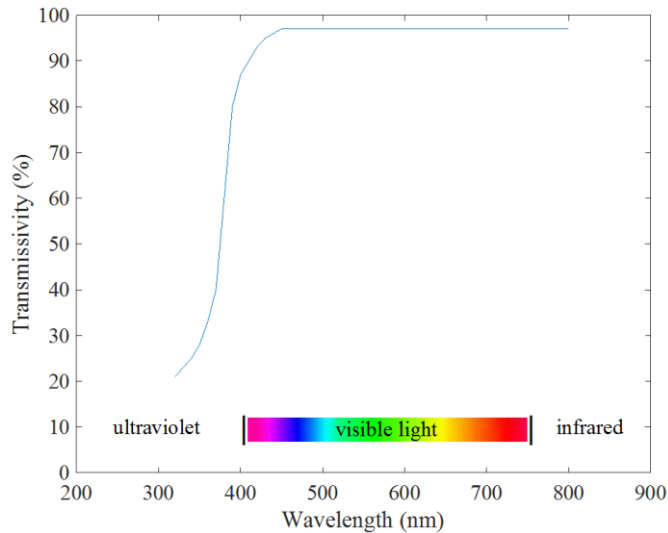
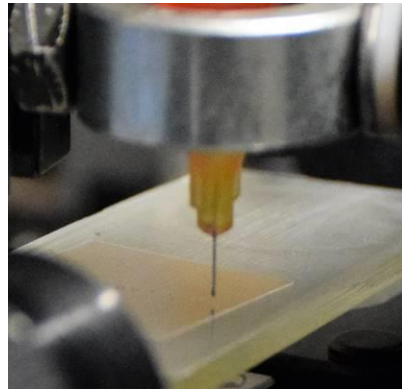


**Figure 3.3** Transmissivity of NOA 68 polymer (as a percent) versus wavelength (in nm). The polymer exhibits low transmission (and thus high absorption) below wavelengths of 420 nm, and for this reason a wavelength of 405 nm is used to cure it. It exhibits high transmission (and thus low absorption) across the visible and near-infrared spectrum, and for this reason it can be used for broadband operation of imaging receivers. The data shown here was provided by Norland Products Inc.

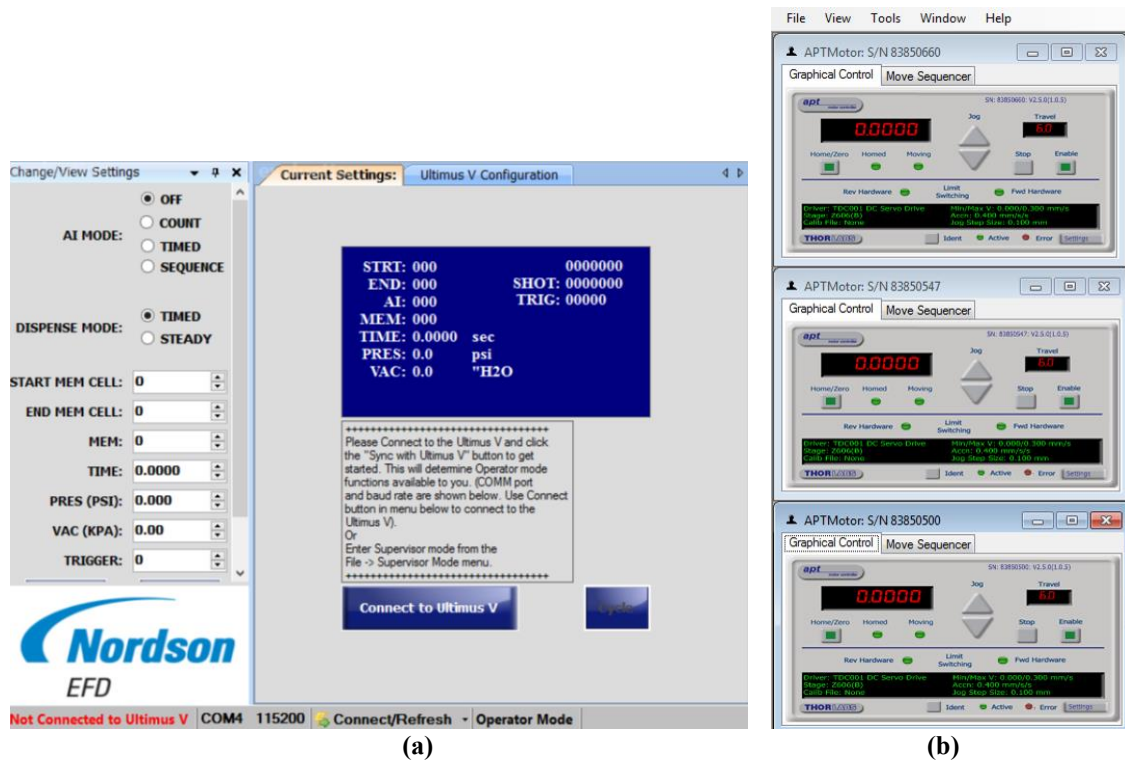


(a)



(b)

Figure 3.4 The microlens dispensing system shown as photographs of (a) the overall system, including the syringe barrel that dispenses the polymer microdroplet and the optical fibre that delivers the UV beam to cure it, and (b) the needle tip that dispenses the polymer to form a microdroplet on the glass substrate.



(a)

(b)

Figure 3.5 The LabVIEW graphical user interfaces for (a) the dispensing sub-system, which controls dispensing polymer into a microdroplet, and (b) the actuation subsystem, which translates the needle tip.

### 3.1.1 Dispensing Sub-System

The dispensing sub-system is responsible for injecting polymer through the needle tip to form a microdroplet on the glass substrate. The sub-system is controlled by LabVIEW software via the user interface shown in Figure 3.5(a). The software activates the pneumatic control unit shown in Figure 3.2, and the pneumatic control unit regulates the pressure applied to the syringe barrel shown in this same figure. The applied pressure forces the piston in the syringe barrel against the polymer, and this dispenses polymer through the needle tip. The pneumatic control unit can output dispensing pressures in the range of 0-100 psi, with dispensing times at or above 100 ms.

The volume of polymer that is dispensed by the pneumatic control unit is an important variable in defining the diameter of the microdroplet and microlens, and this volume is dictated by three key parameters. The first parameter is the size (i.e., gauge) of the needle tip. A small-gauge needle tip, with a large inner diameter, enables the fabrication of relatively large microlenses, on the millimetre-scale. In contrast, a high-gauge needle tip, with a small inner diameter, can be used for both small and large microlenses. This is because the volume of polymer can be adjusted, however needed, by simply changing the dispensing pressure and time. Given the greater capabilities of high-gauge needle tips, and our observations that they yield better reproducibility, 34-gauge needle tips are selected for this work. They have an inner diameter of 80  $\mu\text{m}$ , and in our experience they can fabricate microlenses having diameters down to approximately 160  $\mu\text{m}$  with good reproducibility. The remaining two parameters for the dispensing sub-system are the dispensing pressure and dispensing time. They are chosen according to the characterization shown in Figure 3.6. Figures 3.6(a) and (b) show plots of the microlens diameter,  $d$ , versus dispensing pressure for dispensing in an

ambient (filler) of air and glycerol, respectively. For dispensing in air, the results for dispensing times of 100 ms and 250 ms are denoted by open circles with a grey trendline and crosses with an orange trendline, respectively. For dispensing in glycerol, the results for dispensing times of 1 s and 2.5 s are denoted by open circles with a grey trendline and crosses with an orange trendline, respectively. Dispensing is carried out through the aforementioned 34-gauge needle tip with pressures spanning from 30 psi, below which reproducibility becomes a problem, to 60 psi, being the maximum that can be supplied in the laboratory. The observed trends are logical in that larger pressures and longer dispensing time yield larger microlens diameters. For this study, there is a desire to have microlenses with good reproducibility. Thus, for dispensing in air, a dispensing pressure of 60 psi is used with dispensing times of 100 ms and 250 ms. For dispensing in glycerol, a dispensing pressure of 60 psi is used with a dispensing time of 1s and 2.5s. Intuitively it makes sense that more volume of polymer is required to produce a HCA microlens in comparison to a LCA microlens, therefore the dispensing time in glycerol should be longer.

### **3.1.2 Actuation Sub-System**

The actuation sub-system translates the base upon which the glass substrate lies. The translation is carried out by three orthogonal single-axis motorized actuators (Thorlabs MTS25/M-Z8), with LabVIEW control via the user interface shown in Figure 3.5(b).

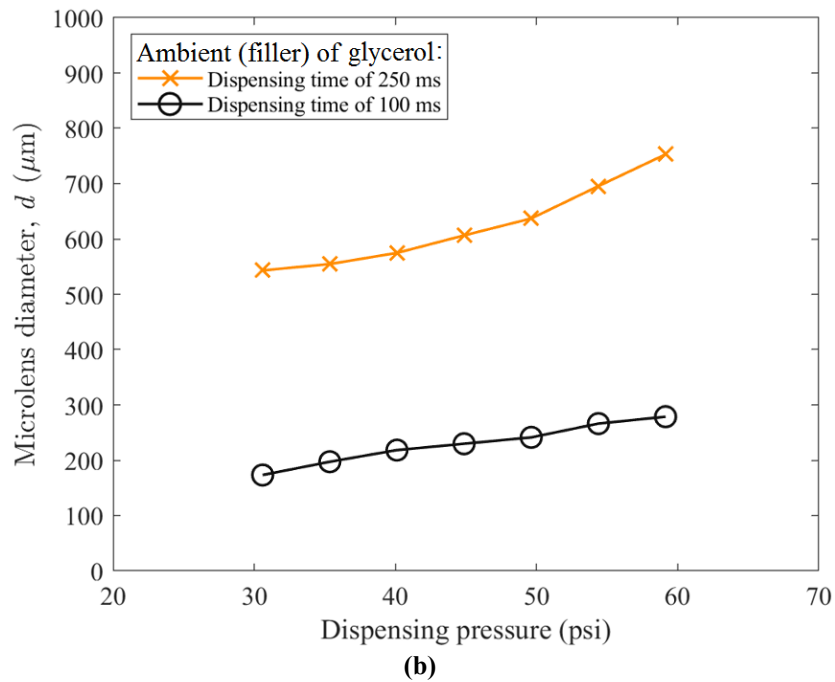
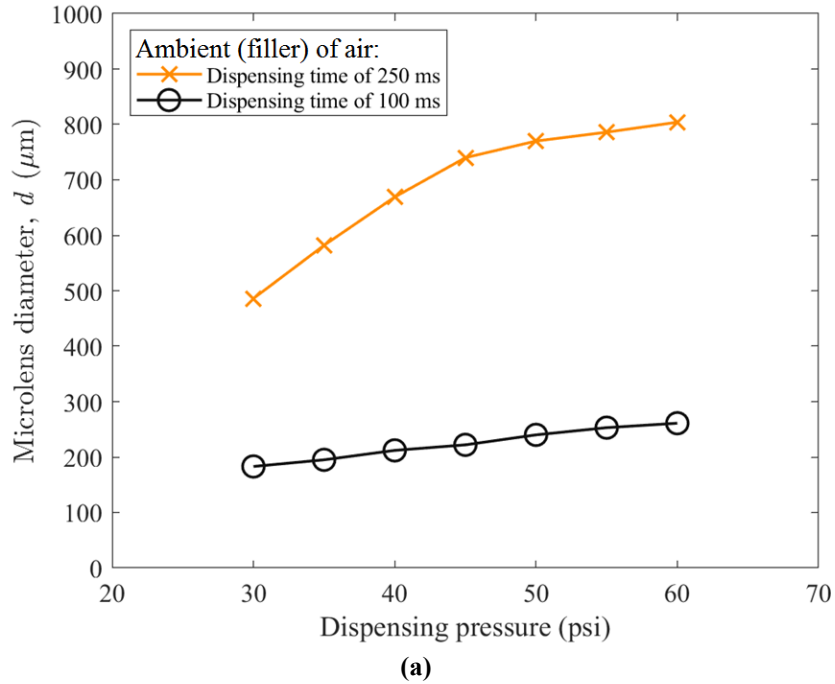
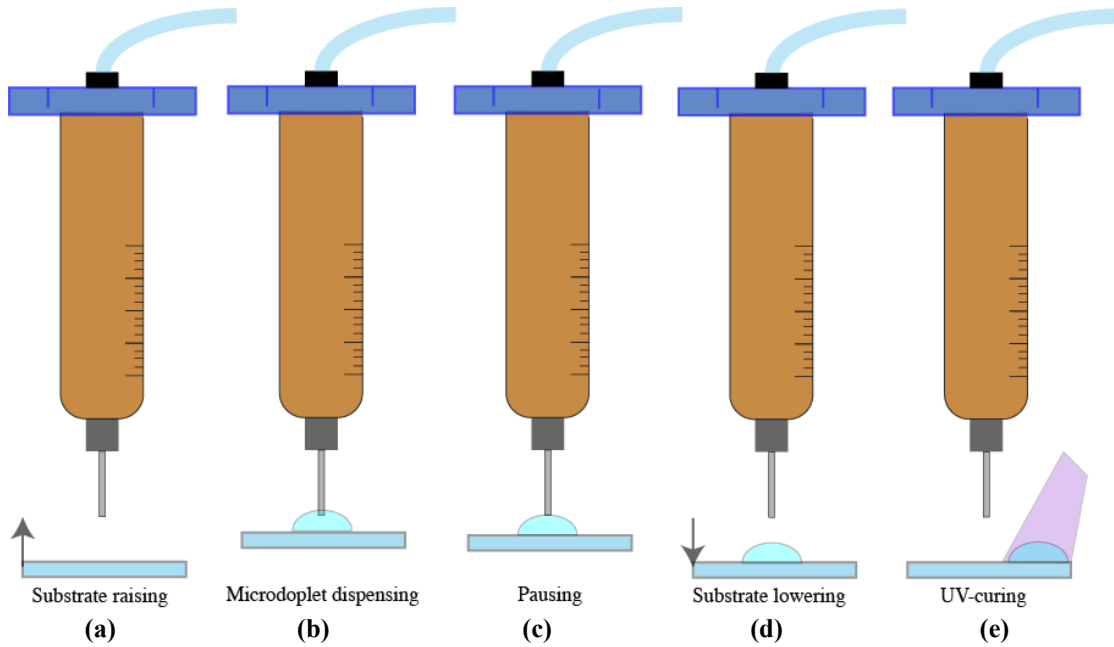


Figure 3.6 Microlens diameter,  $d$ , versus dispensing pressure for dispensing in an ambient (filler) of (a) air and (b) glycerol. A dispensing time of 100 ms is denoted by open circles with a grey trendline; a dispensing time of 250 ms is denoted by crosses with an orange trendline. The dispensing is carried out with a 34-gauge needle tip.

The steps of the actuation sub-system are shown in Figure 3.7. Figure 3.7(a) shows the actuation sub-system raising the glass substrate to set a *relatively large vertical displacement* between the end of the needle tip and the glass substrate. Figure 3.7(b) shows polymer dispensed out of the needle tip via the dispensing sub-system with a set dispensing pressure and time. Figure 3.7(c) shows pausing, over a set pause time. The pause time is equal to the time that pressure is applied, i.e., the dispensing time. This time allows the polymer to spread over the glass substrate, and so it is important in defining the shape of the microlens. Figure 3.7(d) shows the actuation sub-system lowering the glass substrate. Figure 3.7(e) shows UV-curing of the microdroplet over a set curing time.

It is important to note that the above process can also be carried out with some control on the final shape of the microdroplet. This can be seen in the modified steps of the actuation sub-system in Figure 3.8. Figure 3.8(a) shows the actuation sub-system raising the glass substrate to set a *relatively small vertical displacement* between the end of the needle tip and the glass substrate. Figure 3.8(b) shows polymer being dispensed out of the needle tip, as before, but in this case the polymer spreads further out across the glass substrate, due to the smaller vertical displacement between the needle tip and glass substrate. Figure 3.8(c) shows pausing, over a set pause time, to allow the polymer to spread. Figure 3.8(d) shows the glass substrate being lowered by the actuation sub-system. Notice here that contact angle hysteresis and contact line pinning have the microdroplet remain spread out across the substrate with a flattened profile and a relatively low contact angle due to the dispensing here with a small vertical displacement between the end of the needle tip and the glass substrate. Figure 3.8(e) shows UV-curing of the dispensed microdroplet over a set curing time.



**Figure 3.7** Steps of the actuation sub-system for a microdroplet with a relatively high contact angle, due to a relatively large separation between the needle tip and the glass substrate. The steps include (a) substrate raising, (b) microdroplet dispensing, (c) pausing, (d) substrate lowering, and (e) UV-curing.

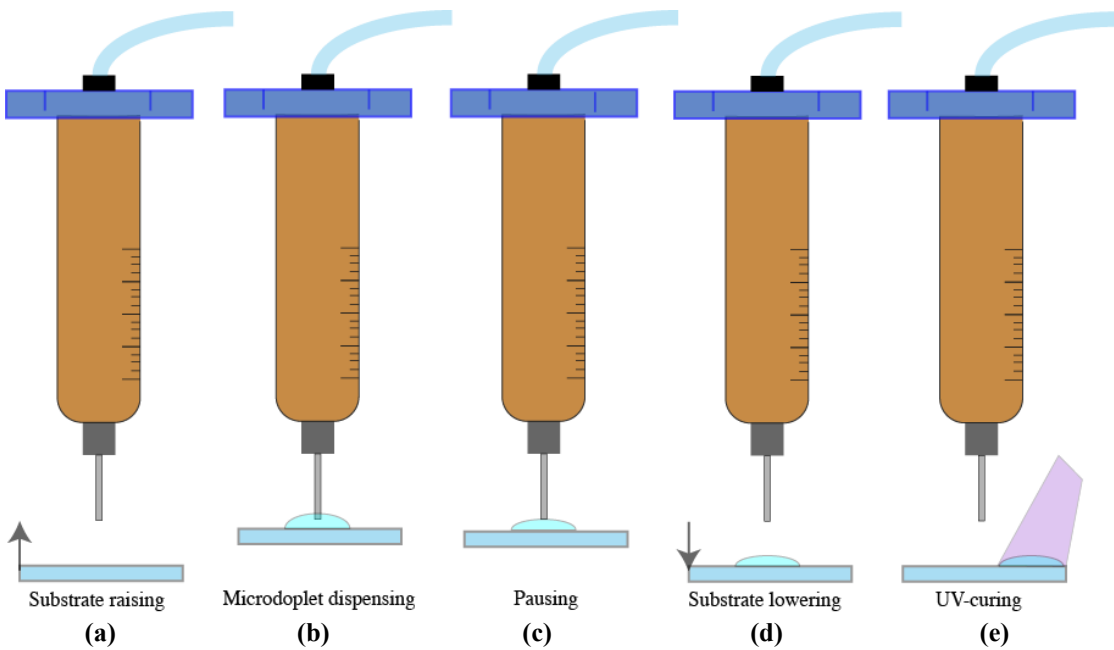


**Figure 3.8** Steps of the actuation sub-system for a microdroplet with a relatively low contact angle, due to a relatively large separation between the needle tip and the glass substrate. The steps include (a) substrate raising, (b) microdroplet dispensing, (c) pausing, (d) substrate lowering, and (e) UV-curing.

There are three key parameters for the above-described actuation sub-system. The first parameter is the vertical displacement between the substrate and needle tip. Numerous arrays of microlenses were dispensed to characterize the dependence of the microlens diameter on this vertical displacement—and identify the displacement that offers the best reproducibility. It was found that a vertical displacement of 10  $\mu\text{m}$  gives the best reproducibility, and so this value was fixed throughout this work. The second parameter is the pause time, attributed to the pausing between the steps of microdroplet dispensing and substrate lowering in Figures 3.7 and 3.8. For this parameter, it is necessary that a sufficiently long pause be applied to allow the microdroplet to spread on the substrate. It was found from experimental characterizations that the pause time can simply be made equal to the dispensing time. This gives longer pauses while dispensing larger microdroplets and yields sufficient reproducibility. The third parameter for the actuation sub-system is the curing time. The process of curing is fairly straightforward in that UV-curing should be applied for a sufficiently long time to realize solidification. (Over-curing was not found to be a problem.) Following experimental characterizations of the curing, it was found that a UV-curing time of 15 s is sufficient. The UV-curing is applied as soon as the substrate is lowered, to prevent the uncured polymer from spreading any further than desired, and it is done through an optical fibre that is aligned in such a way that it does not expose the interior of the needle tip to UV light. It was found that any UV light that exposes the interior of the needle tip can cure the polymer within the tip and thereby narrow its inner diameter. This would lead to a gradual decrease in the volume of polymer being dispensed and sacrifice reproducibility.

## 3.2 Microlens Implementations

This work considers the three microlens implementations proposed in Chapter 2 for application to imaging receivers. The microlenses are formed using the microlens fabrication system introduced in the prior section. The microlens implementations are dispensed onto a glass substrate of a thickness  $t = 200 \mu\text{m}$  before UV curing. For a fair comparison, the cross-sectional areas of the three implementations, as viewed from above, are made equal to have them capture equal optical powers. The fabrication details for the three microlens implementations are described in the following subsections.

### 3.2.1 The Low-Contact-Angle (LCA) Microlens

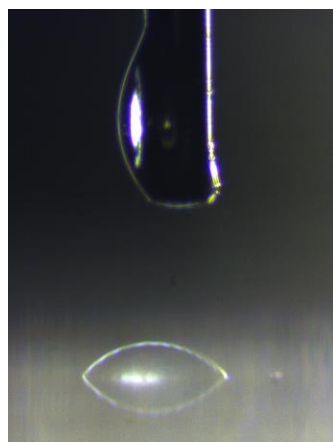
The first microlens implementation considered by this study is the LCA microlens. It is analysed as a benchmark, due to the fact that its low contact angle and imaging characteristics are representative of those achieved by fabrication via the conventional thermal reflow process. The LCA microlens is formed by the microlens fabrication system described in the prior section using the parameters shown in Table 3.1. Of particular note is the fact that the polymer is dispensed in an ambient (filler) of air.

Dispensing in air yields a microlens with a relatively small contact angle, as seen from the photograph in Figure 3.9(a). The microlens has a diameter of  $d = 790 \mu\text{m}$  and contact angle of only  $\alpha = 28.3^\circ$ . This small contact angle is a manifestation of Young's equation, in (6) and (7), for the chosen polymer (NOA 68), substrate (glass), and filler (air). With air as the filler,  $\gamma_{\text{sf}}$  is much larger than  $\gamma_{\text{sl}}$ . This yields a relatively high value for  $\cos\alpha = (\gamma_{\text{sf}} - \gamma_{\text{sl}}) / \gamma_{\text{lf}}$ , which in turn gives a relatively low value for  $\alpha$ .

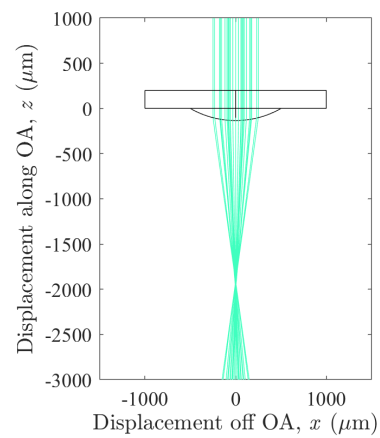
The LCA microlens that is fabricated yields a relatively large normalized focal length and small FOV, as seen in the ray-tracing simulation of Figure 3.9(b). It is important to note from this simulation that the small contact angle manifests itself as a microlens with a large radius of curvature, which in turn produces a large normalized focal length of  $f/d = 2.1$ . The FOV for this fabricated LCA microlens is  $32^\circ$ .

**Table 3.1 Fabrication sub-system parameters for the LCA microlens. The polymer is dispensed for 250ms with a pressure of 60psi while the 32-gauge needle tip is placed 10  $\mu\text{m}$  away from the surface of the glass substrate. After contact of the polymer with the glass substrate in air and the microlens has formed, the UV curing is applied.**

System parameters:		Dispensing sub-system parameters:		Actuation sub-system parameters:	
Microlens (liquid):	NOA 68	Needle tip size:	32-gauge	Vertical displacement:	10 $\mu\text{m}$
Substrate (solid):	Glass	Dispensing pressure:	60 psi	Pause time:	250 ms
Ambient (filler):	Air	Dispensing time:	250 ms	Curing time:	15 s



(a)



(b)

**Figure 3.9 The fabricated LCA microlens as characterized by its (a) photograph, and (b) ray-tracing simulation. The profiles of these two match closely with a total diameter of  $d = 790 \mu\text{m}$ .**

### 3.2.2 The High-Contact-Angle (HCA) Microlens

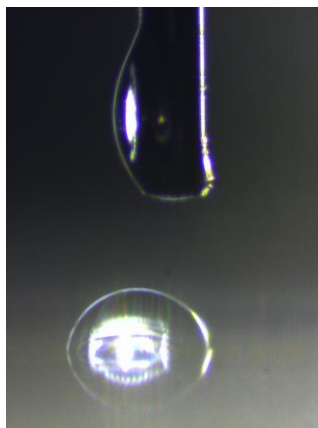
The second microlens implementation of interest to this study is the HCA microlens. It is created by the microlens fabrication system using the parameters shown in Table 3.2. Note that the polymer is dispensed in this case in an ambient (filler) of glycerol rather than air.

Dispensing in glycerol forms the HCA microlens seen in the photograph of Figure 3.10(a). The microlens has a diameter of  $d = 790 \mu\text{m}$  and a contact angle of roughly  $\alpha = 90^\circ$ . Clearly, the use of glycerol as the ambient (filler) here yields a different balance of surface tensions from that of the LCA microlens, which results in a microlens with a much higher contact angle. The polymer (NOA 68) and substrate (glass) are the same as before, and so the surface interfacial energy of  $\gamma_{sl}$  has not changed. However,  $\gamma_{sf}$  has decreased to a value that is comparable to  $\gamma_{sl}$ , to give  $\cos\alpha = (\gamma_{sf} - \gamma_{sl}) = 0$  and  $\alpha = 90^\circ$ .

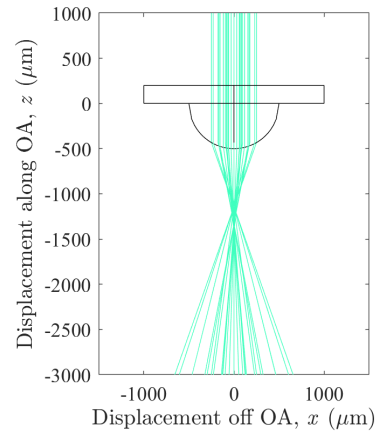
The imaging characteristics of the HCA microlens can be seen in the ray-tracing simulation of Figure 3.10(b). It is apparent here that the larger contact angle of the microlens yields a smaller radius of curvature, which in turn produces a shorter normalized focal length of  $f/d = 1.6$ , in comparison to that of the LCA microlens. The FOV for this fabricated HCA microlens is  $59^\circ$ .

**Table 3.2 Fabrication sub-system parameters for the HCA microlens. The polymer is dispensed for 1.5s with a pressure of 60psi while the 32-gauge needle tip is placed 10  $\mu\text{m}$  away from the surface of the glass substrate. The dispensing takes place in a glycerol filler to achieve the desired contact angle. After contact of the polymer with the glass substrate inside the glycerol and the microlens has formed, the UV curing is applied.**

System parameters:		Dispensing sub-system parameters:		Actuation sub-system parameters:	
Microlens (liquid):	NOA 68	Needle tip size:	32-gauge	Vertical displacement:	10 $\mu\text{m}$
Substrate (solid):	Glass	Dispensing pressure:	60 psi	Pause time:	1.5 s
Ambient (filler):	Glycerol	Dispensing time:	1.5 s	Curing time:	15 s



(a)



(b)

**Figure 3.10 The HCA microlens as characterized by its (a) photograph and (b) ray-tracing simulation. The profiles of these two match closely with a total diameter of  $d = 810 \mu\text{m}$ .**

### 3.2.3 The Low-Contact-Angle (LCA) Microlens Array

The third microlens implementation of interest to this study differs from the prior two implementations in that it is a microlens array. The array takes the form of a  $3 \times 3$  grid of microlenses with a pitch of  $290 \mu\text{m}$ . Each microlens is fabricated by the microlens fabrication

system using the parameters shown in Table 3.3. Note that the polymer is dispensed in an ambient (filler) of air in this case.

The dispensed microlenses within the microlens array are characterized by the photograph in Figure 3.11(a). This figure shows an array of 5x5 microlenses, of which, only the interior 3x3 microlens array is used during characterization in the next chapter. The microlenses have a pitch of 290  $\mu\text{m}$ , a diameter of  $d = 230 \mu\text{m}$ , and an average contact angle of  $\alpha = 28^\circ$ , due to the dispensing in air. The smaller microlens diameter seen here is chosen to yield a total cross-sectional area for the nine microlenses of  $5.1 \times 10^5 \mu\text{m}^2$ , which is comparable to the cross-sectional area of  $4.9 \times 10^5 \mu\text{m}^2$  for the LCA and HCA microlenses. In this way, the imaging receivers using these different implementations of microlenses should capture comparable optical powers and measure similar total signal power.

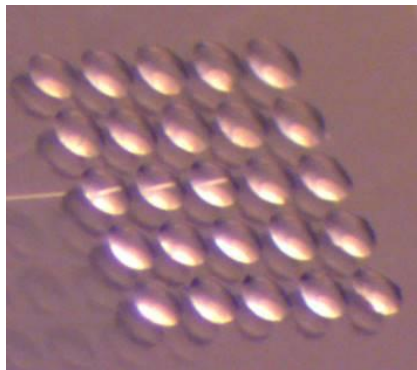
The imaging characteristics of the microlens array are seen in the ray-tracing simulation of Figure 3.11(b). Note here that the use of multiple microlenses with smaller diameters has allowed for focusing over a shorter normalized focal length of  $f/d = 2.1$ , in comparison to that of the LCA microlens. The FOV for this fabricated microlens array is  $30^\circ$ .

There are two points worth mentioning for the microlens array. First, the microlens array is able to achieve the desired flat form factor, by way of a shortened focal length, without a change in the contact angle, as was needed for the HCA microlens. This is because its reduced microlens diameter yields a proportional reduction in the focal length. Second, if desired, the microlens array can be made with even greater numbers of microlenses to increase the captured optical powers and signal levels. Such larger arrays are beyond the scope of this work—which focuses on the physical parameters and imaging characteristics of microlenses within imaging

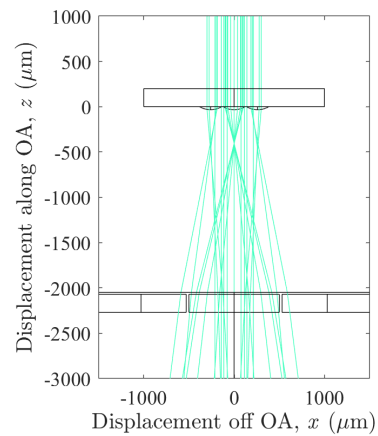
receivers—but details on the fabrication and characterization of large-scale microlens arrays can be found in Appendix B

**Table 3.3 Fabrication sub-system parameters for the LCA microlens array. The polymer is dispensed for 100ms with a pressure of 60psi while the 34-gauge needle tip is placed 10  $\mu\text{m}$  away from the surface of the glass substrate. After contact of the polymer with the glass substrate in air and the microlens has formed, the next element in the array is made. Once all the elements are complete the array is UV cured.**

System parameters:		Dispensing sub-system parameters:		Actuation sub-system parameters:	
Microlens (liquid):	NOA 68	Needle tip size:	34-gauge	Vertical displacement:	10 $\mu\text{m}$
Substrate (solid):	Glass	Dispensing pressure:	60 psi	Pause time:	100 ms
Ambient (filler):	Glycerol	Dispensing time:	100 ms	Curing time:	15 s



(a)



(b)

**Figure 3.11 The LCA microlens array as characterized by its (a) photograph and (b) ray-tracing simulation. The microlens photograph shown is a representative 5x5 microlens array. In characterization, the 3x3 internal microlens array is used for characterization and comparison with the other microlens implementations. In this case, the focal distance seen in the ray-tracing simulations has proportionally decreased focal length due to the smaller diameter.**

### 3.3 Discussion on Reproducibility

The microlens testing in the prior section would benefit from having an HCA microlens array. However, reproducibility is an issue for such arrays. Specifically, the dispensing of polymer microlens in glycerol was found to have poor adhesion onto the glass, and this led to inconsistent results for the microlenses. This was a particularly critical challenge, given that a tight tolerance is needed for the focal lengths in an HCA array. The challenge arises in that microlenses with different focal lengths within the array would produce focal spots of varying sizes on the image sensor, and these variations become accentuated when the contact angle is high and the focal length is short. This ultimately sacrifices the imaging performance.

To quantify the above comments on microlens fabrication reproducibility, 100 samples each of LCA and HCA microlenses were fabricated, with each targeting a diameter of  $d = 230 \mu\text{m}$ . The results are shown in the histogram of Figure 3.12. It shows the number of samples for each measured diameter. It is clear from these results that the LCA microlenses can be fabricated with reasonable accuracy, with the vast majority having diameters between  $225 \mu\text{m}$  and  $235 \mu\text{m}$ . However, the HCA microlenses show far wider variation, with values that span  $225 \mu\text{m}$  to  $265 \mu\text{m}$ , indicating poor precision, as well as heightened values, at a median of  $245 \mu\text{m}$ , indicating poor accuracy.

The challenge of dispensing microlenses in glycerol was the inconsistent adhering of polymer to the glass substrate. The polymer could detach from the glass substrate or adhere to the metal needle tip. This caused dissimilar shapes for the microlenses (at best) or even missing microlenses in an array (at worst). The best results could be achieved by manually controlling the dispensing of polymer for each microlens, but even with such care varying diameters and shapes would result for the HCA microlenses. This can be seen in Figure 3.12.

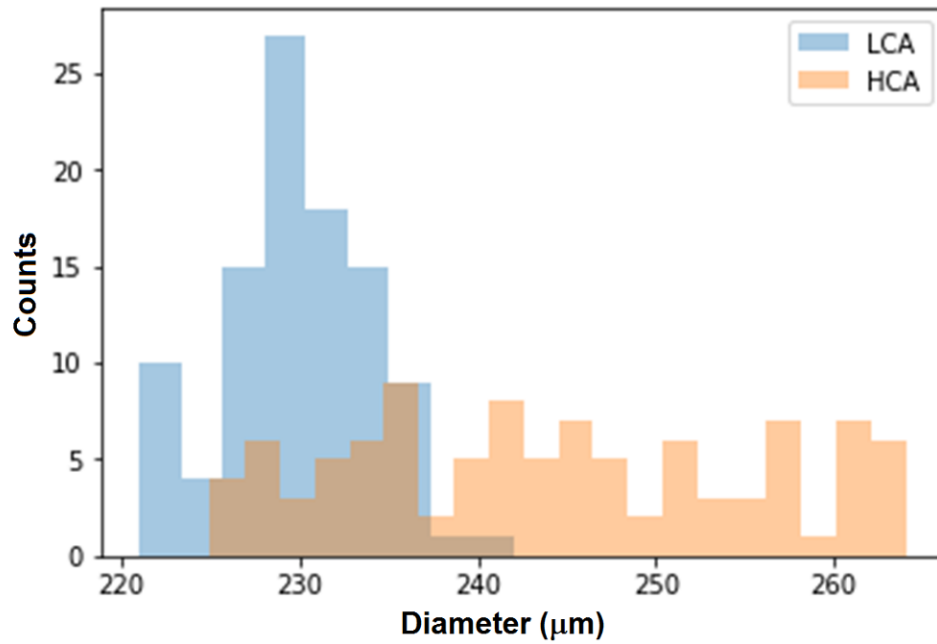


Figure 3.12 Histograms showing the counts for diameters of 100 dispensed LCA and 100 dispensed HCA microlenses. The LCA microlenses denoted by the blue bars show good precision and good accuracy, with values close to the targeted diameter of  $d = 230 \mu\text{m}$ . The HCA microlenses denoted by the orange bars show poor precision and poor accuracy, given their wide variations and heightened values for the diameters.

## Chapter 4: Application of Microlenses to Imaging Receivers

The three implementations of microlenses that were analysed in Chapter 2 and fabricated in Chapter 3 are integrated to make imaging receivers. First, a description and requirements of the imaging receiver is outlined. Secondly, we describe the OW polar angle imaging testbed assembled to evaluate the three imaging receivers. Then, data from the testbed is captured from these integrated imaging receivers. Lastly, the results are discussed and compared by peak intensity for each microlens implementation.

### 4.1 Imaging Receivers

The microlenses that were fabricated are positioned above an image sensor in the manner shown in Figure 4.1. Figures 4.1(a), (b), and (c) show configurations for the LCA microlens, HCA microlens, and LCA microlens array and their relative focal lengths, respectively. The image sensor lies within the focal plane of each microlens, as defined for incident light being parallel to the OA. The focal length is relatively long for the LCA microlens, because it has a low contact angle together with a relatively large diameter. The focal length for the HCA microlens is shorter than that of its LCA counterpart, because its contact angle was made large while its diameter was fixed at that of the LCA microlens. The focal length for the microlens array is even shorter than the prior microlenses, even though it incorporates microlenses with a low contact angle. This is because its focal length is reduced in proportion to its diameter.

The image sensor positioned below the microlenses is an OmniVision OV7720. It is shown in Figure 4.2. The image sensor captures images at a rate of 187 frames-per-second for subsequent processing. It has pixels with a cross-sectional area of  $6 \mu\text{m} \times 6 \mu\text{m}$ .

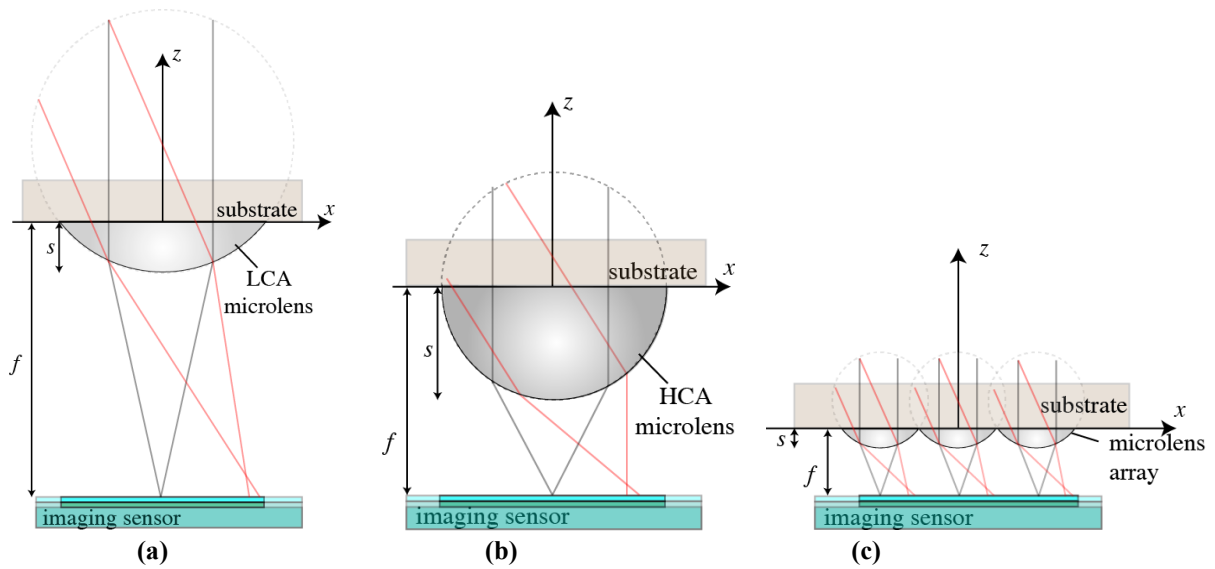


**Figure 4.1** Configurations of the imaging receivers showing the image sensor below the (a) LCA microlens, (b) HCA microlens, and (c) LCA microlens array. The configurations show illumination of the microlenses by light rays that are parallel to the optical axis (in grey) and light rays that are oblique to the optical axis (in red). The oblique rays focus on the image sensor at the outermost edge of the microlens perimeter.

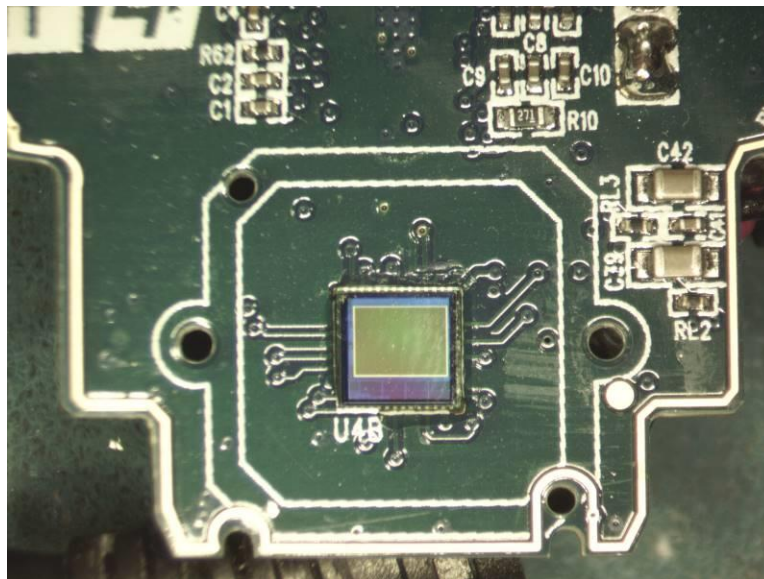


**Figure 4.2** Photograph of the OV7720 image sensor. It captures images at a frame rate of 187 frames-per-second and has pixels with a cross-sectional area of  $6\ \mu\text{m} \times 6\ \mu\text{m}$ .

The image sensor captures an image of the incident intensity on its pixels for subsequent data processing. In this study, the data is imported into and processed by MATLAB<sup>®</sup> using its Image Viewer app. The data is imported as 8-bit values populating three  $640 \times 480$  arrays, with one array for each of the red, blue, and green (RBG) primary colours. The values of the RGB components dictate the perceived colour of a given pixel. For example, a pixel within a captured frame of time with RGB values of  $[0, 0, 0]$ ,  $[255, 0, 0]$ ,  $[0, 255, 0]$ ,  $[0, 0, 255]$ , or  $[255, 255, 255]$  is black, red, green, blue, or white, respectively.

The data structure for the images captured by the image sensor can be visualized in the manner shown in Figure 4.3. The figure shows two-dimensional arrays storing RGB values for each captured frame in time. The captured frames are denoted by  $t_0, t_1, \dots, t_{N-2}, t_{N-1}$ , where the total number of frames is  $N$ . Each RGB array at a given frame in time spans two dimensions, with the integer  $i$  denoting pixel coordinates along the horizontal dimension and the integer  $j$  denoting pixel coordinates along the vertical dimension.

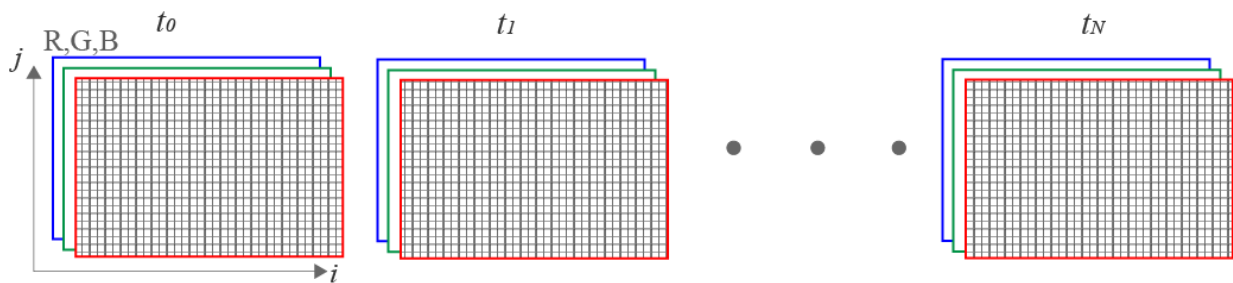


**Figure 4.3** Data structure for the images captured by the image sensor. The captured images are stored as two-dimensional arrays of RGB values at each frame in time. The frames are denoted by  $t_0, t_1, \dots, t_{N-1}$ , where the total number of frames is  $N$ . For each RGB array at a given frame in time, the integers  $i$  and  $j$  denote pixel coordinates along the horizontal and vertical dimensions, respectively.

The algorithm for defining the area of a focal spot on the image sensor and its signal power can be carried out with data from ray-tracing simulations, in accordance with the results of Chapter 2 and with the aid of Figure 4.4. The figure shows intensity profiles on the image sensor from ray-tracing simulations for illumination at the polar angle of  $\theta = 0^\circ$  and the polar angle at the edge of the FOV, being  $\theta = 26^\circ$ ,  $56^\circ$ , and  $26^\circ$  for the LCA microlens in Figure 4.4(a), the HCA microlens in Figure 4.4(b), and the LCA microlens array in Figure 4.4(c), respectively. The figures are shown roughly to scale with pixels having an area of  $6 \mu\text{m} \times 6 \mu\text{m}$ . Each dashed circle denotes the outline of a microlens. Each solid contour line denotes the intensity at half the peak intensity of the given focal spot. As such, the region within each solid contour line is the area over which the intensity is summed to define the signal power of the given focal spot.

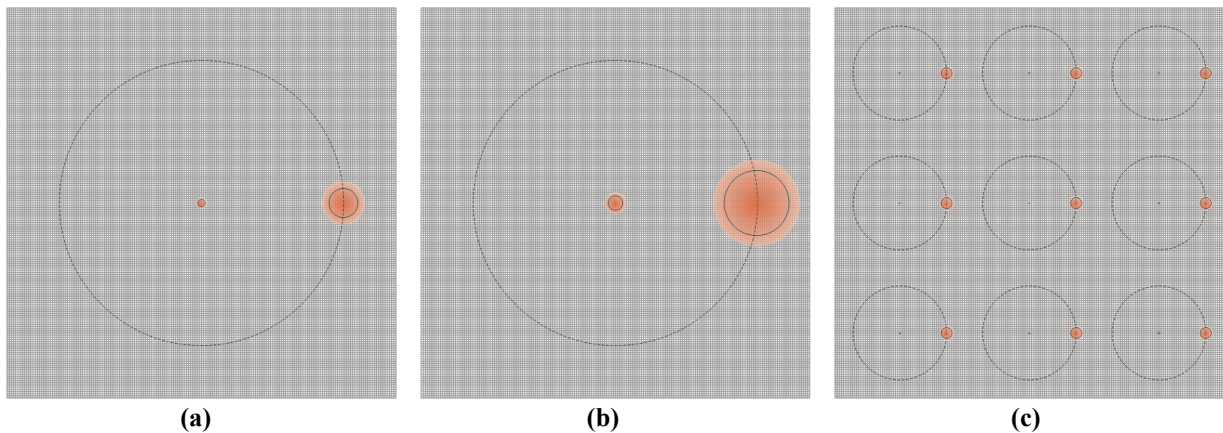


**Figure 4.4 Intensity profiles (in red shading) on the image sensor from ray-tracing analyses for illumination at the polar angle of  $\theta = 0^\circ$  and the polar angle at the edge of the FOV, being  $\theta = 26^\circ$ ,  $56^\circ$ , and  $26^\circ$  for the (a) LCA microlens, (b) HCA microlens, and (c) LCA microlens array, respectively. The results are displayed roughly to scale with a grid of pixels having an area of  $6 \mu\text{m} \times 6 \mu\text{m}$ .**

It is the goal of an imaging receiver to project an image onto the image sensor in such a way that individual transmitters in the environment can be seen and uniquely distinguished. To this end, each focal spot on the image sensor resulting from a given transmitter should have an intensity profile that is as close as possible to a single point. A single point on the imaging receiver would correspond to a single pixel. The diameters chosen in this work led to focal spots that encompass a group of pixels. As such, it became necessary to characterize the focal spot as a finite area on the image sensor.

If the separation between two neighbouring objects is too small, their focal spot will be merged on the focal plane and will be interpreted as a single object by the imaging receiver. The signal power received from a given transmitter can then be taken as the sum of the intensity across the area on the image sensor. If most of this received power is distributed on a pixel area that does not overlap the adjacent transmitter, the object will be spatially distinguishable. Otherwise, if the maximum of one signal overlaps more than half the peak intensity of another signal, it would be spatially indistinguishable. This is shown in Figure 4.5 as intensity profiles of captured images displayed as top and profile views. Figure 4.5(a) shows a case for two objects that are completely isolated and distinguishable. Figure 4.5(b) shows a case where the two objects are in very close proximity, but still distinguishable, in that the two intersect each other at half the peak intensity. This would be the minimum discernable distance. Figure 4.5(c) shows a case where the two objects are too close in proximity, leading to overlapping images and indistinguishable objects.

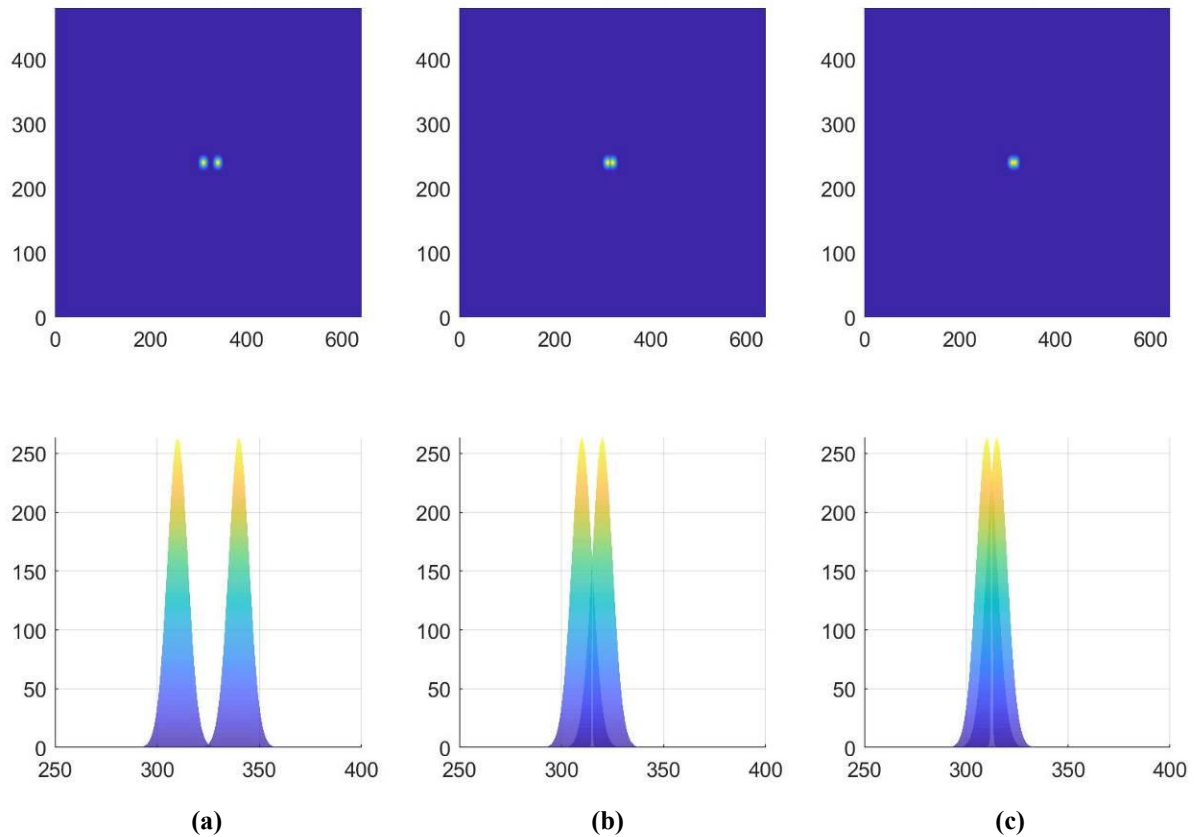


**Figure 4.5 Intensity profiles of two neighbouring LED transmitters focused on the imaging sensor. The top row shows the intensity profiles as viewed from above; the bottom row shows the intensity profiles as viewed in a profile. We see cases here where (a) the two objects are clearly distinguishable, (b) the objects overlap but are still distinguishable, and (c) the two objects produce overlapped images.**

Merging of focal spots will be of critical importance when dealing with microlens arrays. This is because such arrays may have images of adjacent microlenses interfere if the pitch is not large enough. This is not the same issue as the minimum discernable distance, but it will lead to merged signals regardless. In the case where one image overlaps with that of the adjacent microlens in the array, wavelength or frequency multiplexing can be used to allow the processing to distinguish the overlapping signals. Alternatively, the pitch can be increased to create more separation between adjacent microlens and their images.

## 4.2 Optical Wireless Polar Angle Imaging Testbed

The imaging receivers of interest to this study are analysed in an OW testbed with 30 LEDs spread in a hemisphere around the imaging receiver. This setup increases in linear steps the polar angle of  $\Delta\theta = 4^\circ$ , the incident LEDs and maintains a constant radial distance  $R = 50\text{cm}$ . This polar angle imaging testbed can simultaneously test the limits of FOV, the focal distance, and the focal spot size of the LEDs. It varies the incident light in steps of  $\Delta\theta$  over a range from  $\theta = -24^\circ$ , to  $\theta = 96^\circ$ , Figure 4.6 (a) shows the setup with these 30 LEDs spread in the polar angle imaging testbed over the imaging receiver. Figure 4.6 (b) shows the integrated microlens with the image sensor to make the imaging receiver, this image sensor data can be then processed by a computer.

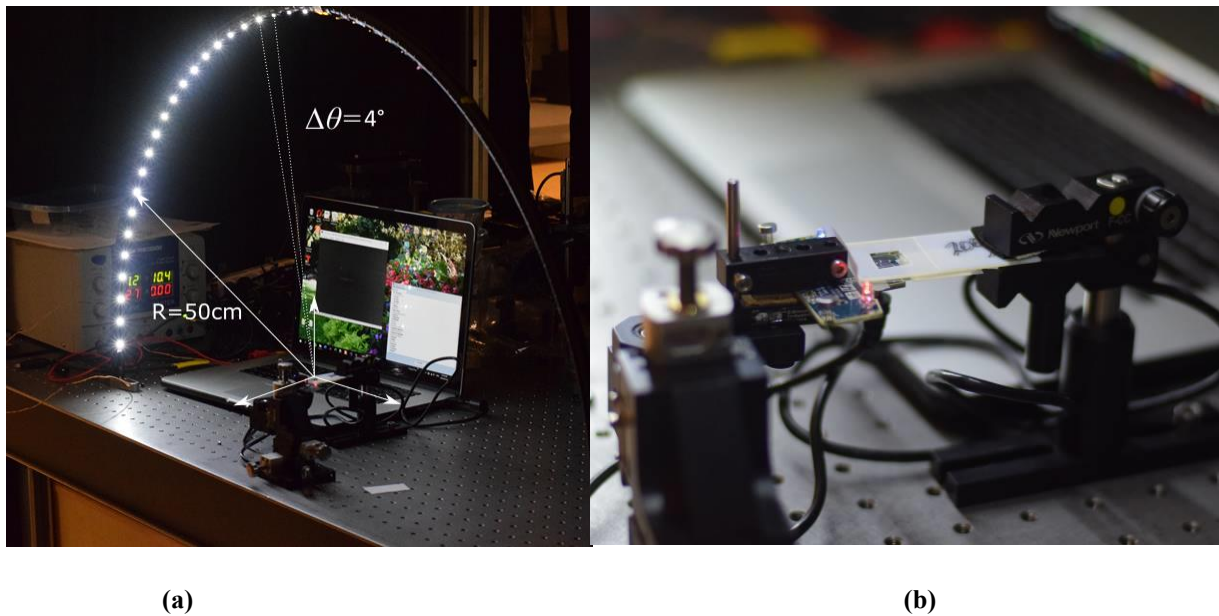


**Figure 4.6 (a) The polar angle imaging testbed with the 30 LEDs transmitters above an imaging receiver. (b) The image sensor integrated with the fabricated microlenses to make the imaging receiver.**

### 4.3 Characterizations of the Imaging Receivers in the Optical Wireless Testbed

The imaging receivers with the differing microlens implementations are subjected to experimental tests, and the results are shown in the following three subsections.

#### 4.3.1 Imaging Receiver with the Low-Contact-Angle (LCA) Microlens

Before characterizing the imaging abilities of the microlenses produced by this fabrication system, single elements are photographed with a scanning electron microscope (SEM). A representative microlens is shown in Figure 4.7(a). The surface of the microlens is seen to be smooth and defect-free. Its contact angle is  $27^\circ$  and its diameter is  $790\ \mu\text{m}$ . Given this low contact angle and large diameter, we would expect to see a long and narrow focal characteristic—according to the ray-tracing simulation in Figure 4.7(b). The LCA microlens is implemented on a glass substrate with the microlens facing the image sensor. Then separation between the microlens and image sensor is adjusted to bring the image of the distant LED transmitters into focus.

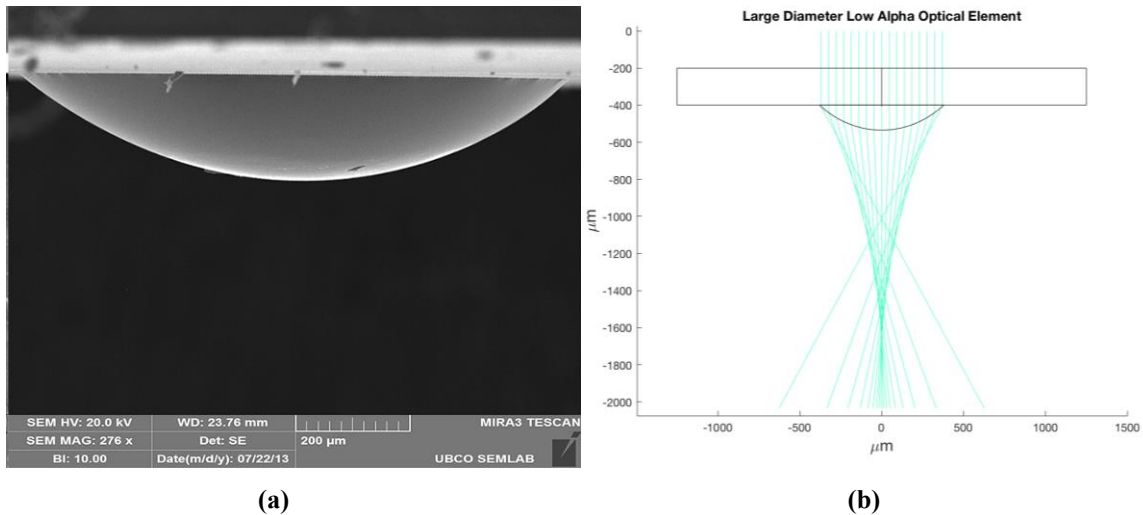


**Figure 4.7** The LCA microlens's (a) SEM image, showing its small contact angle ( $27^\circ$ ) and large diameter ( $790\ \mu\text{m}$ ), and (b) ray-tracing simulation. The microlens was fabricated with a 32-gauge needle tip and 60 psi of pressure for 250 ms. This LCA microlens yields a long and narrow focal characteristic.

The LCA microlens is tested by capturing images of the overhead LED transmitters on the CMOS image sensor and digitizing the results. The images are then processed via Matlab, as data structures with signal levels of the red, green and blue LEDs. Figure 4.8 shows a representative captured image of the 30 overhead LEDs for the LCA microlens. Note the dim LED in the center denoting  $\theta = 0^\circ$ . This maximum experimental FOV is show by the blue intersection of the blue dashed line representing the outline of the microlens. It can be seen it intersects on either side of the dim center point that the blue lines intersects with the fourth LED, which gives  $\theta = 4 \times \Delta\theta = 16^\circ$ , meaning the maximum FOV is  $32^\circ$ , close to the expected.

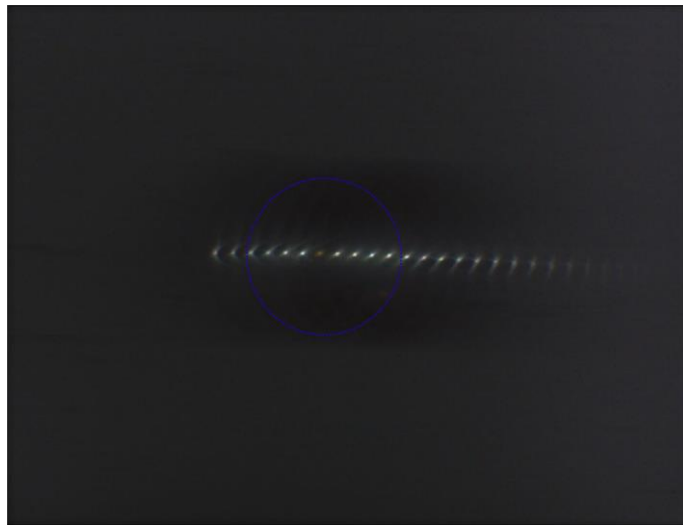


**Figure 4.8** A representative image captured by the image sensor using the LCA microlens. The LCA microlens is capable of resolving sharp focal spots for the displayed five LEDs, but the four LEDs on the corners cannot be captured in the image.

### 4.3.2 Imaging Receiver with the High-Contact-Angle (HCA) Microlens

The implementation and testing of the HCA microlens are similar to those applied for the LCA microlens. An SEM image of the HCA microlens is shown in Figure 4.9(a), and its ray-tracing simulation is shown in Fig. 4.9(b). As was done before, it is mounted about the image sensor with the microlens facing the image sensor. It is found for the focusing of this microlens that the microlens must be much close to the image sensor—as predicted for the higher contact angle. Moreover, it is found that this microlens is far more sensitive to the separation between itself and the image sensor, in comparison to the LCA microlens. This is because the HCA microlens has a shorter depth-of-focus than the LCA microlens (The depth-of-focus scales in proportion to the focal length.).

The HCA microlens is tested by capturing images of the overhead LED transmitters on the CMOS image sensor and digitizing the results. The images are then processed via Matlab, as data structures with signal levels of the red, green and blue LEDs. Figure 4.10 shows a representative image of the 30 overhead LEDs for the HCA microlens. It is interesting to note here that the image sensor is capable of imaging up to 9 LEDs from the center. This leads to a polar incident angle of  $\theta = 9 \times \Delta\theta = 36^\circ$ , which gives a maximum FOV of  $72^\circ$ , a little higher than was expected but within margin of error considering the HCA fabrication process in glycerol that was discussed in Chapter 3.

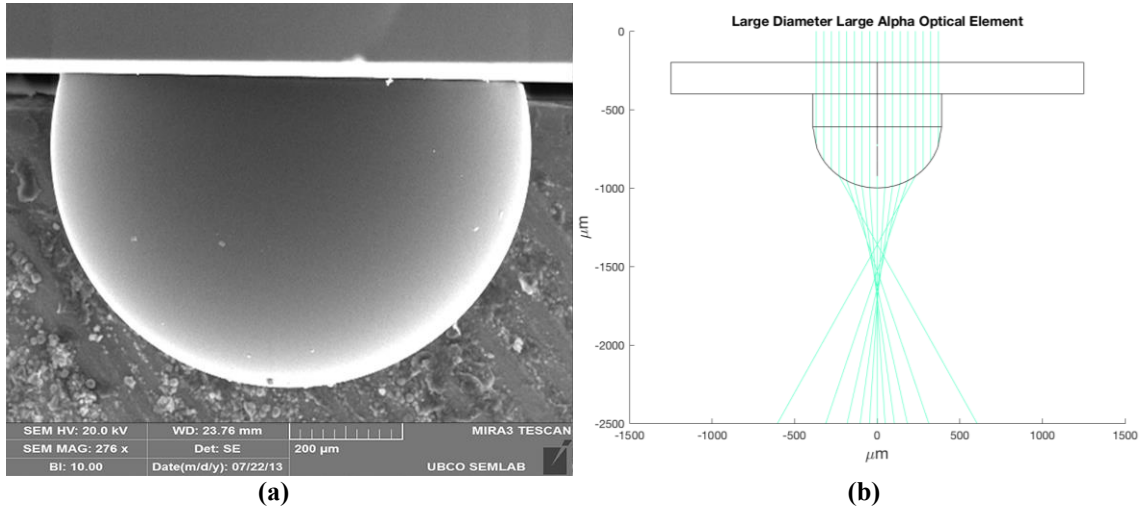


**Figure 4.9** The HCA microlens's (a) SEM image, showing its large contact angle and large diameter (760 μm), and (b) ray-tracing simulation. The microlens was fabricated with a 34-gauge needle tip and 60 psi of pressure for 1 s. This HCA microlens yields a short and wide focal characteristic.

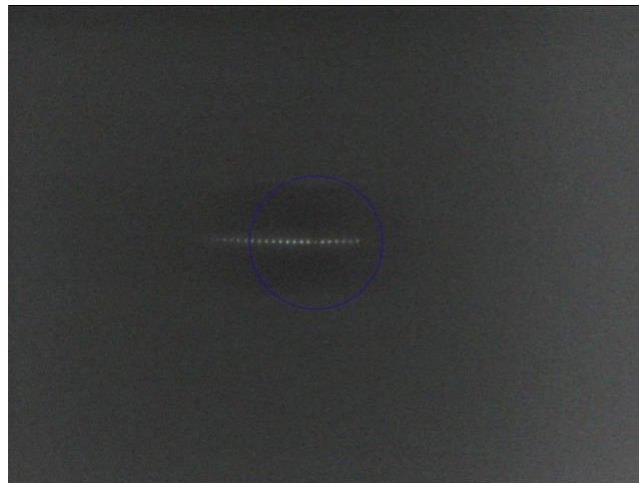


**Figure 4.10** A representative image captured by the image sensor using the HCA microlens. The HCA microlens is capable of resolving sharp focal spots for the displayed five LEDs, but the four LEDs on the corners are not accurately resolved due to aberration.

### 4.3.3 Imaging Receiver with the LCA Microlens Array

The implementation of the LCA microlens array is similar to those applied for the prior two microlenses. It is mounted about the image sensor with the microlenses facing the image sensor. It is then focused. However, the next stage of the analysis did differ from the earlier work. The signal processing for this LCA microlens array was far more challenging than the single-lens cases as the microlens array produces an array of images.

Figure 4.11 shows a representative image of the 30 overhead LEDs for the LCA microlens array. As expected, the FOV does not change with respect to that of the LCA single lens, however the focal length has been greatly reduced due to the reduction in diameter. The challenge with the microlens array is the overlap of images caused by adjacent microlenses. In this case, it is found that the LCA microlens array can capture an image of all the LED transmitters, although their images are not perfectly resolved.

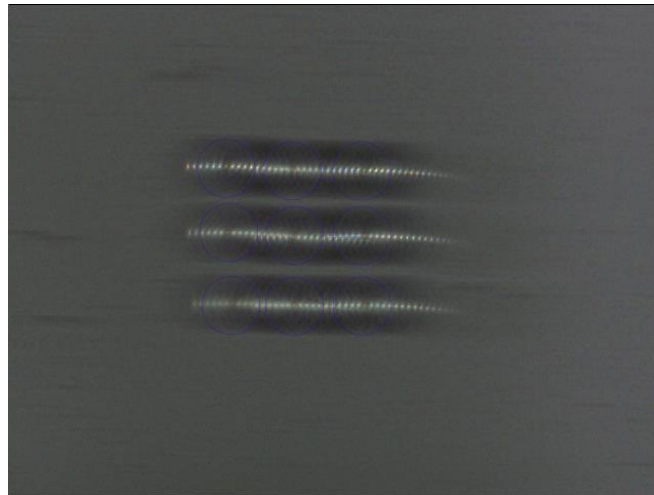


**Figure 4.11** A representative image captured by the image sensor using the LCA microlens array. The LCA microlens array is capable of resolving all the LED transmitters, although their images show large signs of overlap from adjacent microlenses in the array.

#### 4.4 Discussion

In section 4.1, the intensity profiles of focal spots for ray-tracing simulations were shown, and it was suggested that neighbouring objects being imaged must have a sufficiently large separation between them to be distinguishable. In section 4.2, the polar angle imaging testbed was introduced to test the metrics of each microlens implementation. In section 4.3, the imaging results were collected from the integrated imaging receivers using each microlens implementation. In this section, the experimental intensity profiles from the focal spots are compared and discussed.

First, the intensity profile of the integrated imaging receiver with the LCA microlens is shown in Figure 4.12. In this figure, the first subplot in the top left shows the captured and processed image in Matlab. The second subplot in the top right shows the profile of the peak intensity of the projected LED transmitters. The picture on the bottom is a three-dimensional plot showing the pixel peak intensity on the z-axis. The x- and y-axis span the cross-sectional area of the image sensor, with each point on the xy-plane representing a pixel. With the LCA microlens implementation it was predicted that the focal length would be large and the FOV would be narrow. It was also predicted that the LCA microlens would be able to provide small focal spot sizes due to its low spherical and comatic aberration. This characteristic of small focal spot size can be seen with the three-dimensional image in Figure 4.12. With the maximum pixel amplitude being 255, many of the transmitters with small incident polar angles have amplitudes near the maximum value. Moreover, regions between the transmitters are clearly visible, making each LED spatially distinguishable from its neighbours. In this case, the separation between adjacent transmitters on the imaging testbed with a differential polar angle of  $4^\circ$  translates to 14-15 pixels for transmitters near the OA.

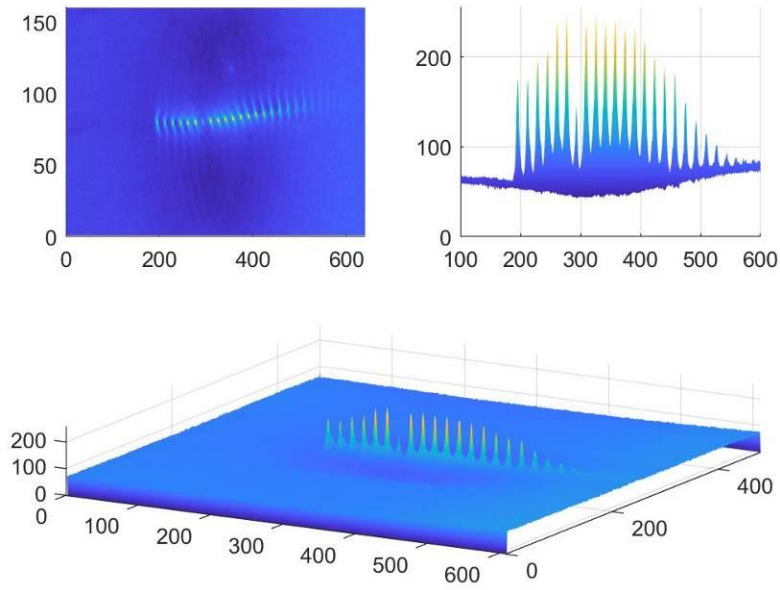


**Figure 4.12** Intensity profile of the captured image with the LCA microlens being implemented in the imaging receiver. This LCA microlens implementation leads to a large spread on the image sensor for the transmitters on the polar angle testbed. This makes it relatively easy for the image sensor to distinguish between neighbouring transmitters as there is a clearly distinguishable peak for each transmitter.

Second, the intensity profile of the integrated imaging receiver with the HCA microlens is shown in Figure 4.13. The same polar angle testbed is used here. By virtue of the high contact angle, and wide FOV, the HCA microlens produces a tight image of the LEDs on the image sensor. After processing, individual transmitters are still clearly distinguishable with clear peaks and valleys in between the focused LEDs. In this case, the separation between the LEDs using a differential polar angle of  $4^\circ$  is between 5-8 pixels near the OA. The characteristics of these spot sizes like those expected from Chapter 2, in that the peak intensity of each individual transmitter is lower, given the increased role of aberration and its increased spread of power on the image sensor (in comparison to that of the LCA).

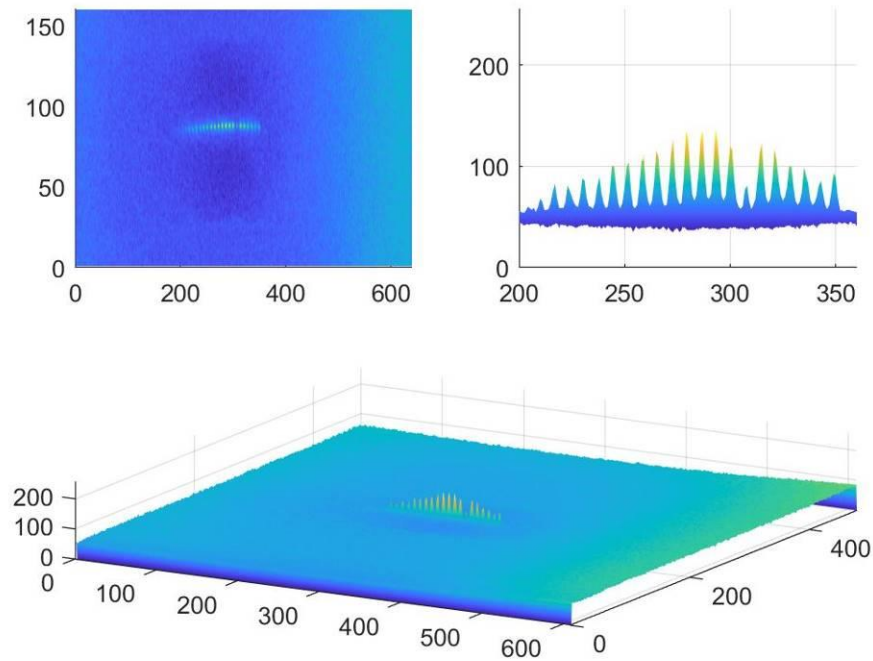


**Figure 4.13** Intensity profile of the captured image with the HCA microlens being implemented in the imaging receiver. This HCA microlens implementation leads to a small spread on the image sensor for the transmitters on the polar angle testbed. However, these spots have smaller peak intensities than those of the LCA due to their aberration and greater spread of power in the focal spot. This makes it more challenging to image process. The challenge arises because it becomes difficult to distinguish between neighbouring transmitters and there is a stronger background level noise (giving a smaller dynamic range).

Last, the intensity profile of the integrated imaging receiver with the LCA microlens array is shown in Figure 4.14. The first subplot shows the captured image of the  $3 \times 3$  array with each microlens in the array having produced its own image from the polar angle imaging testbed. For the second subplot, only one row of three microlenses is extracted to display the peak intensity profiles for three neighbouring microlenses. In this profile, it is noticeable that there are double peaks, showing the effects of overlap in the microlens array.

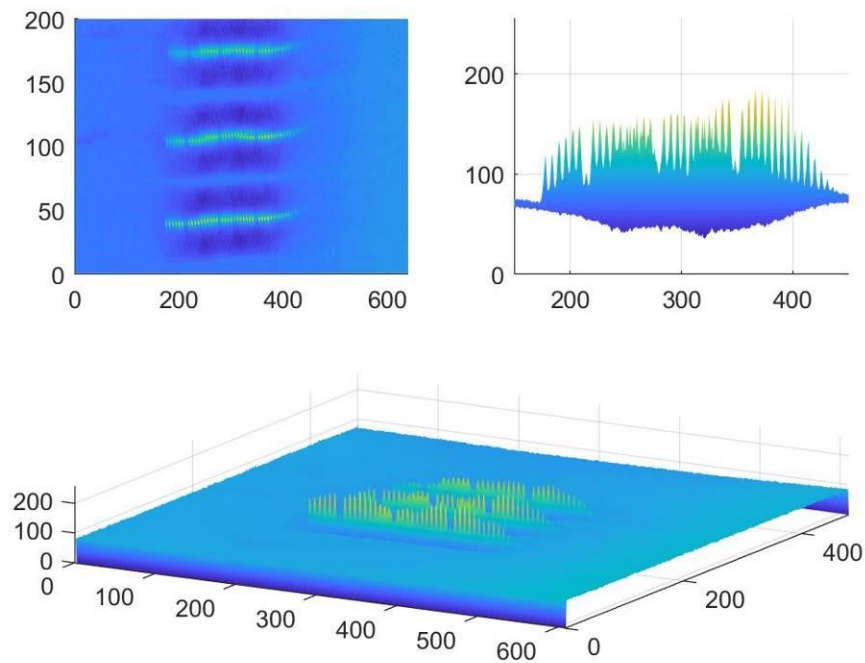


**Figure 4.14 Intensity profile of the captured image with the LCA microlens array being implemented in the imaging receiver. This implementation captures an image with a 3×3 microlens array, with each microlens projecting an image of the transmitters on the polar angle testbed. The replication and overlap of these images can make the signal processing difficult.**

Ultimately, the experimental results shown here confirm the findings and predictions from the simulations in Chapter 2. We see the benefits of the LCA microlens, in that the focal spot remains small and sharp for all angles within its narrow FOV. However, this is not the case for the HCA microlens, which shows a high FOV but a large amount of spherical and comatic aberration. The LCA microlens array offered practical advantages and can ultimately lead to compact imaging receivers. However, it has the downfall of more complex fabrication and signal processing.

## Chapter 5: Conclusion

Within this work, a variety of microlenses were analysed and designed for use in OW systems. A trade-off was found for the design goals in each microlens implementation. The remainder of this chapter summarizes the work and these findings.

In this thesis, we investigated optical microlenses for use in conjunction with image sensors in OW systems. The investigation started with analytical and ray-based analyses in Chapter 2 and continued in Chapter 3 with the development of a microlens fabrication system to implement the microlenses. In Chapter 4, the microlenses that were fabricated were integrated into an OW test bench for experimental testing. It was found that the the LCA microlens could provide small and sharp focal spots for all angles within its FOV. However, the HCA microlens could not do this, because of its spherical and comatic aberration (that appeared in conjunction with its wide FOV). The LCA microlens array could image many widely-distributed LED transmitters, although its image quality/resolution was poor. In practice, the microlens technology that is chosen and applied will need to factor in the exact application being sought for the consumer's electronic device.

Ideas for future work can be divided into improvements for mobile OW communication imaging receivers, improvements for the microlens fabrication system, and improvements for integrating the microlenses with image sensors using custom-made microlenses.

First, it is important to consider the limitation of the imaging receiver. In this thesis, our investigation consisted of the development and integration of microlenses optimized for OW communications. A significant improvement would be the development of an all-optical array of switches as the image sensor. This could enhance the switching speeds of the system.

Secondly, for the fabrication system, there are separate improvements for the actuation subsystem and the curing process. For actuation, there were challenges in the fabrication of large microlens arrays. This was caused by surface roughness on the thin substrate. This surface roughness changes the separation between needle tip and affects the contact line pinning. The change in overall separation can impact the profile of the microlens. A large improvement to this fabrication system would be to regulate the separation between the needle tip and thin substrate, perhaps with a control system, to allow for the same degree of contact line pinning for all microlenses in an array. The curing process can also be implemented in a much more controlled manner. In this thesis, the UV curing was implemented through an optical fibre that directs the incident UV light onto the dispensed NOA polymer. In theory, this curing process could allow for another degree of variability to make customized microlens profiles. A considerable improvement to the fabrication process would be to make the UV curing more precise and accurate. Lastly, the use of apertures for the microlenses would greatly improve the quality of the image captured. Without the use of an aperture, there is light going through the thin substrate, contributing to the collected signal on the image sensor. This appears as ambient noise. For the microlens array, in particular, the space in between the adjacent microlenses could be a significant issue. It is hoped that future work can resolve these issues and ultimately help introduce new forms of OW technology.

## Bibliography

- [1] S. Cherry, "Edholm's law of bandwidth," *IEEE Spectrum*, vol. 41, no. 7, pp. 58–60, 2004.
- [2] Y. Koizumi, K. Toyoda, T. Omiya, M. Yoshida, T. Hirooka, and M. Nakazawa, "512 QAM transmission over 240 km using frequency-domain equalization in a digital coherent receiver," *Optics Express*, vol. 20, no. 21, p. 23383, Oct. 2012.
- [3] D. C. O'Brien *et al.*, "High-speed integrated transceivers for optical wireless," *IEEE Communications Magazine*, vol. 41, no. 3, pp. 58–62, Mar. 2003.
- [4] B. Glushko, D. Kin, and A. Shar, "High bandwidth optical wireless network for gigabit communication," in *2013 IEEE Global High Tech Congress on Electronics*, Shenzhen, 2013, pp. 114–120.
- [5] K. Suzuki, M. Nakazawa, E. Yamada, and Y. Kimura, "5Gbitps, 250km error-free soliton transmission with Er Doped Fibre Amplifiers and Repeaters," *Electronics Letters*, vol. 26, no. 8, p. 551, Apr. 1990.
- [6] R. X. G. Ferreira *et al.*, "High Bandwidth GaN-Based Micro-LEDs for Multi-Gb/s Visible Light Communications," *IEEE Photonics Technology Letters*, vol. 28, no. 19, pp. 2023–2026, Oct. 2016.
- [7] D. Milovančev, T. Jukić, B. Steindl, P. Brandl, and H. Zimmermann, "Optical wireless communication using a fully integrated 400  $\mu\text{m}$  diameter APD receiver," *The Journal of Engineering*, vol. 2017, no. 8, pp. 506–511, Aug. 2017.

- [8] K. D. Dambul, D. C. O'Brien, and G. Faulkner, "Indoor Optical Wireless MIMO System With an Imaging Receiver," *IEEE Photonics Technology Letters*, vol. 23, no. 2, pp. 97–99, Jan. 2011.
- [9] P. Djahani and J. M. Kahn, "Analysis of Infrared Wireless Links Employing Multibeam Transmitters and Imaging Diversity Receivers," *IEEE TRANSACTIONS ON COMMUNICATIONS*, vol. 48, no. 12, p. 12, 2000.
- [10] H. Chun *et al.*, "LED Based Wavelength Division Multiplexed 10 Gb/s Visible Light Communications," *Journal of Lightwave Technology*, vol. 34, no. 13, pp. 3047–3052, Jul. 2016.
- [11] H. M. Oubei, C. Li, K.-H. Park, T. K. Ng, M.-S. Alouini, and B. S. Ooi, "23 Gbit/s underwater wireless optical communications using directly modulated 520 nm laser diode," *Optics Express*, vol. 23, no. 16, p. 20743, Aug. 2015.
- [12] S. Arnon, "Pointing error statistics," in *Advanced Optical Wireless Communication Systems*, S. Arnon, J. Barry, G. Karagiannidis, R. Schober, and M. Uysal, Eds. Cambridge: Cambridge University Press, 2012, pp. 87–89.
- [13] T. Komine, S. Haruyama, and M. Nakagawa, "A Study of Shadowing on Indoor Visible-Light Wireless Communication Utilizing Plural White LED Lightings," *Wireless Personal Communications*, vol. 34, no. 1–2, pp. 211–225, Jul. 2005.

- [14] R. X. G. Ferreira *et al.*, “High Bandwidth GaN-Based Micro-LEDs for Multi-Gb/s Visible Light Communications,” *IEEE Photonics Technology Letters*, vol. 28, no. 19, pp. 2023–2026, Oct. 2016.
- [15] Popvic, Z. D., Sprague, R. A. and Connel, G. A. N., “Technique for monolithic fabrication of microlens arrays,” *Appl. Opt* 27 (7), p. 1281-1284, 1988.
- [16] S. Di and R. Du, “The controlling of microlens contour by adjusting developing time in the thermal reflow method,” presented at the International Symposium on Photoelectronic Detection and Imaging 2009, Beijing, China, 2009, p. 73811D.
- [17] B. E. A. Saleh and M. C. Teich, *Fundamentals of photonics*, 2nd ed. Hoboken, N.J: Wiley Interscience, 2007.
- [18] “Microlens array fabrication by enhanced thermal reflow process: Towards efficient collection of fluorescence light from microarrays.”
- [19] M.-K. Park *et al.*, “Design and Fabrication of Multi-Focusing Microlens Array with Different Numerical Apertures by using Thermal Reflow Method,” *Journal of the Optical Society of Korea*, vol. 18, no. 1, pp. 71–77, Feb. 2014.
- [20] J. L. Cruz-Campa, M. Okandan, M. L. Busse, and G. N. Nielson, “Microlens rapid prototyping technique with capability for wide variation in lens diameter and focal length,” *Microelectronic Engineering*, vol. 87, no. 11, pp. 2376–2381, Nov. 2010.

- [21] M. Mortazavi and M. Nosonovsky, “Adhesion, Wetting, and Superhydrophobicity of Polymeric Surfaces,” in *Polymer Adhesion, Friction, and Lubrication*, H. Zeng, Ed. Hoboken, NJ, USA: John Wiley & Sons, Inc., 2013, pp. 177–226.
- [22] S. Vafaei and M. Z. Podowski, “Theoretical analysis on the effect of liquid droplet geometry on contact angle,” *Nuclear Engineering and Design*, vol. 235, no. 10–12, pp. 1293–1301, May 2005.
- [23] S. K. Rhee, “Surface energies of silicate glasses calculated from their wettability data,” *Journal of Materials Science*, vol. 12, no. 4, pp. 823–824, Apr. 1977.
- [24] L. Gao and T. J. McCarthy, “Contact Angle Hysteresis Explained,” *Langmuir*, vol. 22, no. 14, pp. 6234–6237, Jul. 2006.

## Appendices

### Appendix A - Lens Aberration Types

In this appendix the details of the different types of aberration on the microlens are explained and visualized through simulations. Noise sources and distortion can be specific to different environments, and image sensors, respectively. However, aberration is closely tied with the research carried out in this thesis, in relation to microlenses and optical elements. Therefore, it is worth a deeper explanation of the effects of different types of aberration, and how it can be mitigated.

#### Spherical Aberration

As the name suggests, this aberration is caused due to the spherical profile of the lens. As the distance from the optical axis increases, the incident light is refracted sharper and sharper, effectively changing the focal length as a function of the distance from optical axis. A way to mitigate this is by using an aperture and essentially blocking the outside rays causing the early focus to occur.

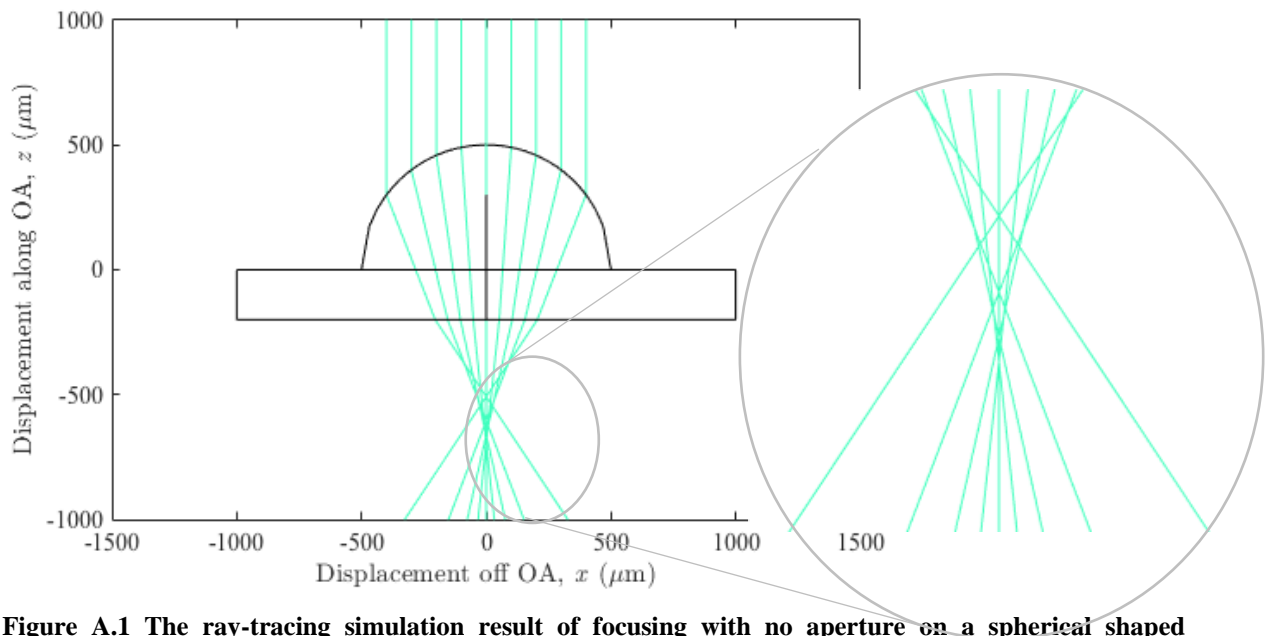


**Figure A.1** The ray-tracing simulation result of focusing with no aperture on a spherical shaped microlens with the incident rays parallel to the optical axis (OA). Showing the outside incident rays focusing earlier than the rays closer to the OA.

## Comatic Aberration

Comatic aberration manifests itself with larger incident angles with spherical microlenses. It manifests itself as an asymmetric focal spot in the image plane with a high density of rays close to the OA and a low density of rays far from the OA. Thus, the focal spot in the transverse image plane resembles a comet—with a highest intensity focal spot close to the OA and a low-intensity tail flaring away from the OA

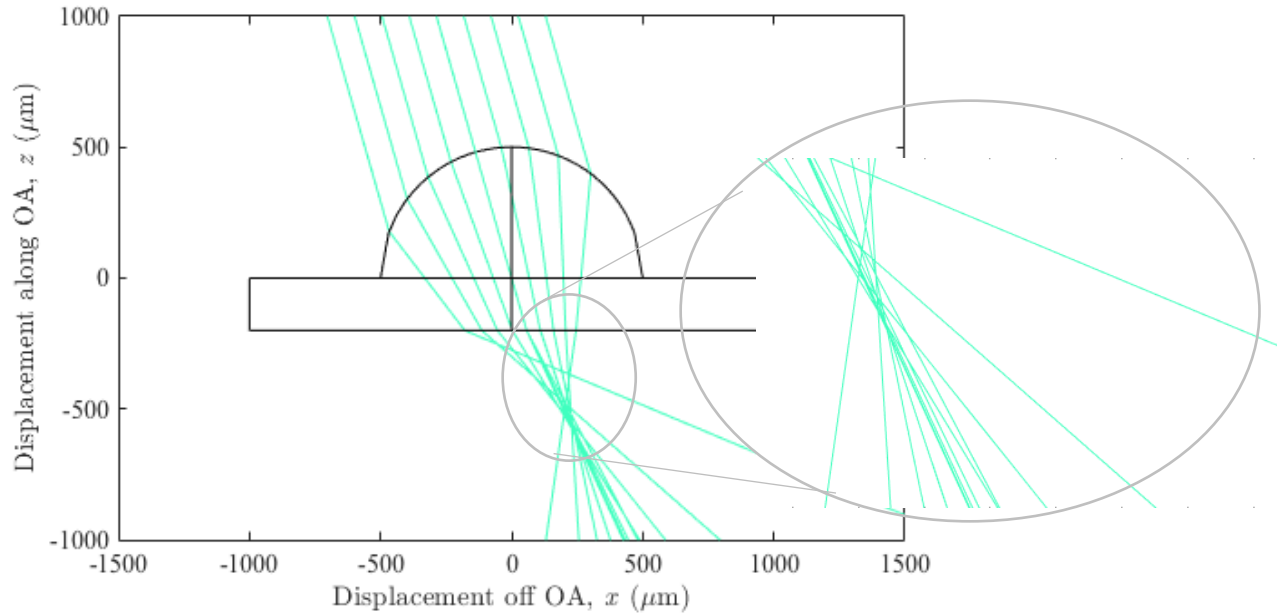


**Figure A.2** The ray-tracing simulation result of focusing with a shaped microlens with the incident rays coming at an angle larger than  $\theta = 0^\circ$  (OA). Showing the inside incident rays getting refracted in such a way to produce a comet like profile.

## Appendix B - Microlens Array Fabrication

This appendix explains the collaborations with industry partner Recon Instruments which allowed for further research into fabricating microlens arrays of different types. This company specializes in heads up displays (HUD) for eyewear applications. The end goal was to find a way to improve the optics of the HUD by using integral microlens array techniques.

The final ambitious goal was split into smaller stages. The initial goal during this project was first to establish a fabrication system that can yield repeatable microlenses during fabrication so that they exhibit the same imaging characteristics for arrays of  $n \times n$  size, such as the 40x40 shown in Figure B.1. In addition, the second challenge was to create not only the convex portion of the dispensed microlens array, but to use the dispensed array as a mold to make a concave array out of similar PDMS resin. Lastly, it was required to integrate two different microlens arrays in such a way to achieve integral imaging.

A large part of this project was characterizing the focal lengths of these microlenses using the setup showing in Figure B.2.



**Figure B.1 A fabricated 40x40 MLA with microlens diameters of 180  $\mu\text{m}$  and a 240  $\mu\text{m}$  pitch between adjacent microlenses.**

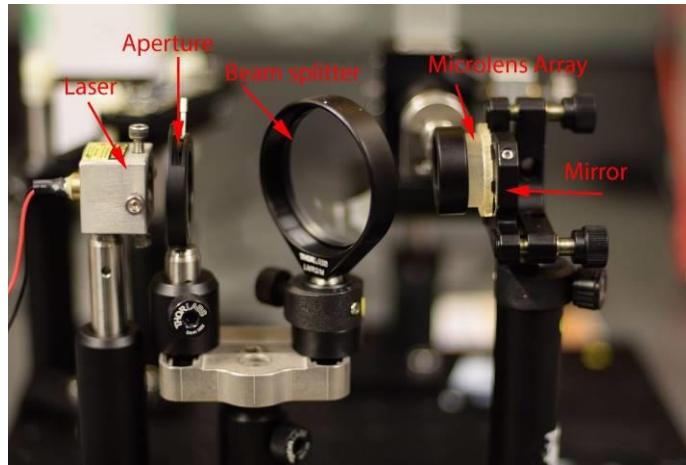


**Figure B.2 Configuration with laser to measure the focal length of the microlens arrays. The laser comes in as a collimated beam and is focused onto the mirror, which reflects the light back to the microlens to have it collimated again and shot through the beam splitter.**